A Hybrid Spectral and Finite Element Method for Coseismic and Postseismic Deformation

Tomáš Pergler, Ctirad Matyska

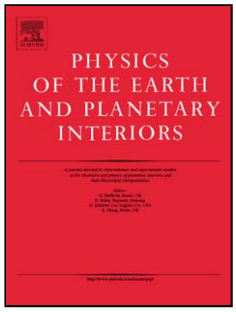

Title: A Hybrid Spectral and Finite Element Method for Coseismic and Postseismic Deformation

Authors: Tomáš Pergler, Ctirad Matyska

PII: S0031-9201(07)00121-5
DOI: doi:10.1016/j.pepi.2007.05.012
Reference: PEPI 4838

To appear in: *Physics of the Earth and Planetary Interiors*

Received date: 15-1-2007
Revised date: 26-5-2007
Accepted date: 27-5-2007

Please cite this article as: Pergler, T., Matyska, C., A Hybrid Spectral and Finite Element Method for Coseismic and Postseismic Deformation, *Physics of the Earth and Planetary Interiors* (2007), doi:10.1016/j.pepi.2007.05.012

A Hybrid Spectral and Finite Element Method for Coseismic and Postseismic Deformation

Tomáš Pergler and Ctirad Matyska

Department of Geophysics, Faculty of Mathematics and Physics, Charles University, V Holešovičkách 2, 180 00 Prague 8, Czech Republic

Abstract

We investigate the elastic and viscoelastic responses of the Earth to a sudden slip along a fault. Firstly, equations describing the Earth's infinitesimal deformations for elastic and viscoelastic rheological models are introduced within the weak formulation and the theorems of existence and uniqueness of solutions are demonstrated. Three-dimensional numerical method, which combines the 2-D finite element method in a plane perpendicular to the fault with application of the Fourier transform in the direction along the fault, is described. We then discuss several numerical benchmarks. At the end, the coseismic deformation and the Coulomb stress for the August 14, 2003 earthquake on the Lefkada island in Greece are computed incorporating also the influence of topography. We demonstrate that the results are sensitive to both source interpretations and the epicenter area topography.

Keywords: weak formulation, finite element method, spectral decomposition, seismic source, Coulomb stress, topography effect.

1 Introduction

Various computational methods have been proposed for postseismic viscoelastic relaxation modelling. The simplest models consisting, for example, of an elastic layer over a homogeneous viscoelastic medium can be solved analytically or semi-analytically for both Cartesian and spherical geometries (e.g. Singh and Rani, 1993, 1994; Yu et al., 1996; Sun and Okubo, 2002; Sun, 2004; Singh and Singh, 2004; Hetland and Hager, 2005). Multilayered Maxwellian models are usually studied by means of the normal mode technique, which was originally developed for postglacial rebound modelling (Pollitz, 1992, 1997, 2003; Piersanti et al., 1995, 1997; Sabadini and Vermeersen, 1997; Soldati et el., 1998, 2001; Boschi et al., 2000; Cesca et al., 2000; Nostro et al., 2001; Melini et al., 2004). In the case of fully 3-D rheology or complicated geometrical structures, a local numerical method is needed. The most popular is the 3-D finite element method (FEM), which was employed in various models (Yoshioka and Tokunaga, 1998; Yoshioka and Suzuki, 1999; Suito and Hirakara, 1999; Suito et al., 2002; Hu et al., 2004; Cianetti et al., 2005) is, in general, also suitable for contact problems of complex fault system (e.g. Xing and Mora, 2006, Xing et al., 2006).

However, in many common geological situations, variations of the rheological structures in the horizontal direction along a fault are negligible (or unknown). The aim of this study is to demonstrate that in such cases 2-D finite elements in the vertical plane perpendicular to the faults can be successfully combined with spectral decomposition in the remaining horizontal direction. We will first deal with an elastic coseismic response to a 2-D general slip along a fault and then we will study postseismic relaxation of Maxwellian rheological models.

In order to obtain reliable numerical method we start with the weak formulation of the corresponding system of partial differential equations including also the proofs of existence and uniqueness of the solution. Our effort is then concentrated to the numerical implementation of 2-D linear finite elements combined with the 1-D Fourier transform; results of several benchmarks are demonstrated. At the end we also present computations of the Coulomb stress distribution for selected Greek earthquakes including topographical effects.

The description of the problems including equations and formulations are presented in sections 2 and 3, the weak formulation is mentioned in section 4 and the detailed proofs are explained in appendix. In section 5, the theoretical approach of spectral decomposition is introduced. Section 6 describes the employed slip function and numerical methods and the results are demonstrated in section 7.

2 Fundamental Equations

Equation of Motion

The linearized equation of motion for a solid, which can be found e.g. in Dahlen (1998), is given by

$$\nabla \cdot \boldsymbol{\tau} - \rho_0 \left[\nabla\varphi_1 + 2\boldsymbol{\omega} \times \partial_t \boldsymbol{u} + \partial_{tt}\boldsymbol{u} - (\nabla \cdot \boldsymbol{u}) g_0 \boldsymbol{e}_r + \nabla(g_0 \boldsymbol{u} \cdot \boldsymbol{e}_r)\right] = 0, \quad (2.1)$$

where $\boldsymbol{u}$ denotes displacement, $\boldsymbol{\tau}$ is the incremental Cauchy stress tensor and φ_1 stands for changes of the gravitational potential due to deformation. The coefficient ρ_0 is a reference density of the Earth, g_0 is its gravitational acceleration, ω is the angular frequency of rotation of the Earth, the vector $\boldsymbol{e}_r$ is a radial unit vector pointing from center of the Earth and $\partial_t \boldsymbol{u}(\partial_{tt}\boldsymbol{u})$ denotes first (second) partial derivatives with respect to time.

In this section we introduce the equations that are used to describe the deformation of the elastic and viscoelastic inhomogeneous Earth. The Earth is considered to be a deformed body with pre-stress caused by hydrostatic pressure and self-gravitation. However, we will not deal with wave phenomena in this study and thus both the inertial force $\rho_0 \partial_{tt}\boldsymbol{u}$ and the Coriolis force $-\rho_0 2\boldsymbol{\omega} \times \partial_t \boldsymbol{u}$ will be omitted. Moreover, in regional studies the self-gravitation, which is described by the term $-\rho_0 \nabla\varphi_1$, can be also neglected.

Rheological Models

To complete the description of the Earth behavior, we consider two alternative rheological models. One of them is the elastic rheology given by Hooke's law

$$\boldsymbol{\tau} - \lambda(\nabla \cdot \boldsymbol{u})\boldsymbol{I} - 2\mu\, \boldsymbol{\varepsilon}(\boldsymbol{u}) = 0, \quad (2.2)$$

where λ and μ represent the elastic Lamé coefficients, $\boldsymbol{I}$ is the identity tensor and $\boldsymbol{\varepsilon}$ is the small strain tensor.

The second relation is for the Maxwell viscoelastic rheology given by the formula

$$\frac{\partial}{\partial t}\boldsymbol{\tau} - \frac{\partial}{\partial t}\left[\lambda(\nabla \cdot \boldsymbol{u})\boldsymbol{I} + 2\mu\, \boldsymbol{\varepsilon}(\boldsymbol{u})\right] + \frac{\mu}{\eta}\left[\boldsymbol{\tau} - K(\nabla \cdot \boldsymbol{u})\boldsymbol{I}\right] = 0, \quad (2.3)$$

where η denotes the dynamic viscosity.

The small strain tensor $\boldsymbol{\varepsilon}(\boldsymbol{u})$ is defined as

$$\boldsymbol{\varepsilon}(\boldsymbol{u}) = \frac{1}{2}\left(\nabla \boldsymbol{u} + (\nabla \boldsymbol{u})^T\right). \quad (2.4)$$

The bulk modulus K can be expressed as the linear combination of Lamé coefficients

$$K = \lambda + \frac{2}{3}\mu. \tag{2.5}$$

3 Formulation of the Problem in Cartesian Geometry

We are dealing with elastic and viscoelastic response of the Earth to a slip along a fault. Even for large earthquakes the fault extent is not larger than tens of kilometers and thus the curvature of the area, which is used for our numerical computations, can be neglected.

Elastic Problem

We aim to solve the system of equations

$$\nabla \cdot \boldsymbol{\tau} + \rho_0 \left[(\nabla \cdot \boldsymbol{u}) g_0 \boldsymbol{e}_z - \nabla (g_0 \boldsymbol{e}_z \cdot \boldsymbol{u}) \right] = 0 \qquad \text{in } \Omega, \tag{3.1a}$$

$$\boldsymbol{\tau} - \lambda (\nabla \cdot \boldsymbol{u}) \boldsymbol{I} - 2\mu\, \boldsymbol{\varepsilon}(\boldsymbol{u}) = 0 \qquad \text{in } \Omega, \tag{3.1b}$$

for the unknown incremental displacement $\boldsymbol{u} = \boldsymbol{u}(\boldsymbol{x})$ and the incremental stress $\boldsymbol{\tau} = \boldsymbol{\tau}(\boldsymbol{x})$. Domain $\Omega \subset R^3$ is bounded and has a Lipschitz boundary. The vector $\boldsymbol{e}_z$ is a unit vector pointing upward in the direction of the z-coordinate. The coefficients ρ_0, g_0 are assumed to depend only on z.

As it is shown in Figure 1, the external boundary of the domain Ω is divided into parts Γ_1 and Γ_2. The equations are then followed by the boundary conditions

$$\boldsymbol{\tau}(\boldsymbol{x}) \cdot \boldsymbol{n} = 0 \qquad \text{on } \Gamma_1, \tag{3.2a}$$

$$\boldsymbol{u}(\boldsymbol{x}) = 0 \qquad \text{on } \Gamma_2, \tag{3.2b}$$

where the vector $\boldsymbol{n}$ is the outward unit normal to $\partial\Omega$ and the sets Γ_1 and Γ_2 are non-empty and open with respect to $\partial\Omega$. The first condition describes a free-surface. The second condition corresponds to the fact that for sufficiently huge computational domain Ω the displacement is very small on the subterranean boundaries of Ω.

The slip is introduced by means of the inner boundary condition

$$[\boldsymbol{u}(\boldsymbol{x}) \cdot \boldsymbol{n}]^+_- = 0 \qquad \text{on } \Gamma, \tag{3.3a}$$

$$[\boldsymbol{u}(\boldsymbol{x}) - (\boldsymbol{u}(\boldsymbol{x}) \cdot \boldsymbol{n})\, \boldsymbol{n}]^+_- = \boldsymbol{f}_\Gamma(\boldsymbol{\xi}) \qquad \text{on } \Gamma, \tag{3.3b}$$

$$[\boldsymbol{\tau}(\boldsymbol{x}) \cdot \boldsymbol{n}]^+_- = 0 \qquad \text{on } \Gamma, \tag{3.3c}$$

where $\boldsymbol{\xi}$ denotes a coordinate vector in the fault plane and the vector $\boldsymbol{n}$ is the unit normal to the fault Γ.

We then require the continuity of the normal component of displacement and of all components of the fraction, whereas $\boldsymbol{f}_\Gamma$ describes the slip along the fault.

Viscoelastic Problem

The second problem is time-dependent for the case when the Earth behaves like a Maxwell viscoelastic body. We have thus the following system of equations

$$\nabla \cdot \boldsymbol{\tau} + \rho_0 \left[(\nabla \cdot \boldsymbol{u}) g_0 \boldsymbol{e}_z - \nabla (g_0 \boldsymbol{e}_z \cdot \boldsymbol{u}) \right] = 0 \qquad \text{in } \Omega \times I, \tag{3.4a}$$

$$\partial_t \boldsymbol{\tau} - \partial_t \left[\lambda (\nabla \cdot \boldsymbol{u}) \boldsymbol{I} + 2\mu\, \boldsymbol{\varepsilon}(\boldsymbol{u}) \right] + \frac{\mu}{\eta} \left[\boldsymbol{\tau} - K (\nabla \cdot \boldsymbol{u}) \boldsymbol{I} \right] = 0 \qquad \text{in } \Omega \times I, \tag{3.4b}$$

where the unknowns $\boldsymbol{u} = \boldsymbol{u}(\boldsymbol{x}, t)$ and $\boldsymbol{\tau} = \boldsymbol{\tau}(\boldsymbol{x}, t)$ are now time-dependent. $I = [0, T],\ T > 0$, is the considered time interval. All the coefficients ρ_0, g_0, λ, μ, K and η are considered to be time independent.

The equations (3.4a), (3.4b) are solved for the initial conditions

$$\boldsymbol{u}(\boldsymbol{x}, 0) = 0 \qquad \text{in } \Omega, \tag{3.5a}$$

$$\boldsymbol{\tau}(\boldsymbol{x}, 0) = 0 \qquad \text{in } \Omega, \tag{3.5b}$$

the boundary conditions (3.2a), (3.2b) and the slip conditions (3.3a) - (3.3c) which now holds for all $t \in [0, T]$.

4 Weak Formulation of the Problems and Existence and Uniqueness Theorems

Elastic Problem

Because of the discontinuity of the solution inside the area Ω it is reasonable to split a function $\boldsymbol{u}$ to two parts

$$\boldsymbol{u} \equiv \begin{cases} \overline{\boldsymbol{u}} + \boldsymbol{f} & \text{in } \Omega_f, \\ \overline{\boldsymbol{u}} & \text{in } \Omega_f^C = \Omega \setminus \overline{\Omega}_f, \end{cases} \tag{4.1}$$

where $\Omega_f \subset \overline{\Omega}_f \subset \Omega$ is a domain of non-zero measure, which is located on the one side to the fault and particular shape of this domain is arbitrary. Let $\boldsymbol{f}$ be a function, which fulfill these conditions

$$T_\Gamma \boldsymbol{f} = \boldsymbol{f}_\Gamma \qquad \textit{and} \qquad T_{\partial\Omega_f \setminus \Gamma} \boldsymbol{f} = 0, \tag{4.2}$$

where T denotes the trace operator.

Definition 4.1 *Let*

$$V \equiv \left\{ \boldsymbol{v} \in [W^{1,2}(\Omega)]^3; \boldsymbol{v}\big|_{\Gamma_2} = 0 \right\}. \tag{4.3}$$

where $W^{1,2}(\Omega)$ denotes the Sobolev space [1]*. We say that function $\boldsymbol{u} = \overline{\boldsymbol{u}} + \boldsymbol{f}$ is a weak solution of the problem (3.1)-(3.3) if*

$$\begin{aligned}
&\overline{\boldsymbol{u}} \in V \\
&\boldsymbol{f} \in \left[W^{1,2}(\Omega_f)\right]^3 \textit{ satisfies the conditions (4.2) and} \qquad (4.4a)\\
&\int_\Omega \left[2\mu\ \boldsymbol{\varepsilon}(\overline{\boldsymbol{u}}) : \boldsymbol{\varepsilon}(\boldsymbol{U}) + \lambda(\nabla\cdot\overline{\boldsymbol{u}})(\nabla\cdot\boldsymbol{U})\right]\ \mathrm{d}x \\
&+ \int_\Omega \rho_0 \left[\nabla(g_0 \boldsymbol{e}_z \cdot \overline{\boldsymbol{u}}) - (\nabla\cdot\overline{\boldsymbol{u}}) g_0 \boldsymbol{e}_z\right]\cdot \boldsymbol{U}\ \mathrm{d}x \\
&= -\int_{\Omega_f} 2\mu\ \boldsymbol{\varepsilon}(\boldsymbol{f}) : \boldsymbol{\varepsilon}(\boldsymbol{U})\ \mathrm{d}x - \int_{\Omega_f} \lambda(\nabla\cdot\boldsymbol{f})(\nabla\cdot\boldsymbol{U})\ \mathrm{d}x \\
&- \int_{\Omega_f} \rho_0 \left[\nabla(g_0 \boldsymbol{e}_z \cdot \boldsymbol{f}) - (\nabla\cdot\boldsymbol{f}) g_0 \boldsymbol{e}_z\right]\cdot \boldsymbol{U}\ \mathrm{d}x \qquad \forall \boldsymbol{U} \in V \qquad (4.4b)
\end{aligned}$$

Theorem 4.2 (Existence and Uniqueness of the Elastic Problem) *Let the space V be defined by (4.3) and furthermore, let*

$$P \equiv \left\{ \boldsymbol{A} \in \left[L^2(\Omega)\right]^{3\times 3}; \boldsymbol{A} = \boldsymbol{A}^T \right\}. \tag{4.5}$$

Let the following conditions hold [2],[3]*:*

- $\mu, \lambda, \rho_0 \in L^\infty(\Omega), \quad g_0 \in W^{1,\infty}(\Omega), \quad \boldsymbol{f} \in \left[W^{1,2}(\Omega_f)\right]^3$ *satisfies (4.2)*
- $0 \le \lambda(\boldsymbol{x}), \quad 0 < \mu_0 \le \mu(\boldsymbol{x}) \qquad$ *almost everywhere (a.e.) in* Ω
- $0 < C_{ab} := 2\mu_0 C_K - (1+\sqrt{3}) \left\|\rho_0\right\|_\infty \left\|g_0\right\|_{1,\infty}$

[1] Sobolev space $W^{1,2}(\Omega)$ stand for square integrable vector functions with square integrable derivatives and the scalar product $(\boldsymbol{u}, \boldsymbol{v}) = \int_\Omega (\boldsymbol{u}\boldsymbol{v} + \nabla\boldsymbol{u} : \nabla\boldsymbol{v})\, dx$, where : denotes the total scalar product of tensors.

[2] C_K is a constant which occurs in Korn's inequality

[3] The space $L^\infty(\Omega)$ contains just all measurable functions on Ω and $W^{1,\infty}(\Omega)$ is the space of function from $L^\infty(\Omega)$ with measurable derivatives.

Then the problem (4.3), (4.4) has a solution $\overline{\boldsymbol{u}} \in V$ *which depends on the function* $\boldsymbol{f}$*. For one particular slip* $\boldsymbol{f}_\Gamma$ *we have a unique solution* $\boldsymbol{\tau} \in P$ *and* $\boldsymbol{u} \equiv \overline{\boldsymbol{u}} + \boldsymbol{f}$*.*

Proof: See the appendix.

Viscoelastic Problem

For the viscoelastic problem we have the following weak formulation:

Definition 4.3 *We say that the functions* $\boldsymbol{u} = \overline{\boldsymbol{u}} + \boldsymbol{f}$ *and* $\boldsymbol{\tau} = \boldsymbol{\sigma} + \lambda(\nabla \cdot \boldsymbol{u})\boldsymbol{I} + 2\mu\,\boldsymbol{\varepsilon}(\boldsymbol{u})$ *represent a weak solution of the viscoelastic problem (3.3)-(3.5) if*

$$\begin{aligned} &\overline{\boldsymbol{u}} \in W^{1,2}\left((0,T);V\right) \\ &\boldsymbol{\sigma} \in L^2\left((0,T);P\right) \quad , \quad \partial_t\boldsymbol{\sigma} \in L^2\left((0,T);P\right) \\ &\boldsymbol{f} \in \left[W^{1,2}\left(\Omega_f\right)\right]^3 \end{aligned}$$

where $W^{1,2}\left((0,T);V\right)$ *and* $L^2\left((0,T);P\right)$ *denotes Bochner spaces* [4]*. Further the functions* $\overline{\boldsymbol{u}}$ *and* $\boldsymbol{\sigma}$ *satisfy the equations*

[4]Given a measure space $(T, \mathcal{F}, \mu)$, a Banach space $(X, \|\cdot\|_X)$ and $1 \le p \le +\infty$, the Bochner space $L^p(T;X)$ is defined to be the space of all measurable functions $u : T \to X$ such that the corresponding norm is finite:

$$\|u\|_{L^p(T;X)} := \left(\int_T \|u(t)\|_X^p \,\mathrm{d}\mu(t)\right)^{1/p} < +\infty \quad for \quad 1 \le p < \infty.$$

The Bochner space $W^{p,q}(T;X)$ can be defined similarly way.

$$\int_\Omega \left[2\mu\ \boldsymbol{\varepsilon}(\overline{\boldsymbol{u}}) : \boldsymbol{\varepsilon}(\boldsymbol{U}) + \lambda(\nabla\cdot\overline{\boldsymbol{u}})(\nabla\cdot\boldsymbol{U})\right]\ \mathrm{d}x$$
$$+\int_\Omega \rho_0\left[\nabla(g_0\boldsymbol{e}_z\cdot\overline{\boldsymbol{u}}) - (\nabla\cdot\overline{\boldsymbol{u}})g_0\boldsymbol{e}_z\right]\cdot\boldsymbol{U}\ \mathrm{d}x + \int_\Omega \boldsymbol{\sigma} : \boldsymbol{\varepsilon}(\boldsymbol{U})\ \mathrm{d}x$$
$$= -\int_{\Omega_f} 2\mu\ \boldsymbol{\varepsilon}(\boldsymbol{f}) : \boldsymbol{\varepsilon}(\boldsymbol{U})\ \mathrm{d}x - \int_{\Omega_f}\lambda(\nabla\cdot\boldsymbol{f})(\nabla\cdot\boldsymbol{U})\ \mathrm{d}x$$
$$-\int_{\Omega_f}\rho_0\left[\nabla(g_0\boldsymbol{e}_z\cdot\boldsymbol{f}) - (\nabla\cdot\boldsymbol{f})g_0\boldsymbol{e}_z\right]\cdot\boldsymbol{U}\ \mathrm{d}x \qquad \forall\boldsymbol{U}\in V \tag{4.6a}$$

$$\int_\Omega \partial_t\boldsymbol{\sigma} : \boldsymbol{\mathcal{S}}\ \mathrm{d}x + \int_\Omega \frac{\mu}{\eta}\boldsymbol{\sigma} : \boldsymbol{\mathcal{S}}\ \mathrm{d}x$$
$$+\int_\Omega 2\ \frac{\mu^2}{\eta}\boldsymbol{\varepsilon}(\overline{\boldsymbol{u}}) : \boldsymbol{\mathcal{S}}\ \mathrm{d}x - \int_\Omega \frac{2}{3}\ \frac{\mu^2}{\eta}(\nabla\cdot\overline{\boldsymbol{u}})\,\mathrm{Tr}\,\boldsymbol{\mathcal{S}}\ \mathrm{d}x$$
$$= -\int_{\Omega_f} 2\ \frac{\mu^2}{\eta}\boldsymbol{\varepsilon}(\boldsymbol{f}) : \boldsymbol{\mathcal{S}}\ \mathrm{d}x + \int_{\Omega_f}\frac{2}{3}\ \frac{\mu^2}{\eta}(\nabla\cdot\boldsymbol{f})\,\mathrm{Tr}\,\boldsymbol{\mathcal{S}}\ \mathrm{d}x \qquad \forall\boldsymbol{\mathcal{S}}\in P \tag{4.6b}$$

$$\textit{for a.e. } t\in(0,T)$$

with the initial condition

$$\boldsymbol{\sigma}(\boldsymbol{x},0) = 0 \qquad \textit{in } \Omega. \tag{4.7}$$

Theorem 4.4 (Existence and Uniqueness of the Viscoelastic Problem)

Assume that the same conditions as in the case of the elastic problem are satisfied and furthermore let

$$\exists\eta_0: \quad 0<\eta_0\le\eta(\boldsymbol{x}) \quad \textit{a.e. in } \Omega.$$

Then the problem (4.6),(4.7) has a solution $\overline{\boldsymbol{u}}$ *which depends on function* $\boldsymbol{f}$ *and for one particular slip* $\boldsymbol{f}_\Gamma$ *we have a unique solution* $\boldsymbol{u}$, $\boldsymbol{\tau}$ *and* $\boldsymbol{\sigma}$. *Moreover,*

$$\overline{\boldsymbol{u}}\in\mathcal{C}\left([0,T];V\right), \quad \boldsymbol{\tau}\in\mathcal{C}\left([0,T];P\right), \quad \boldsymbol{\sigma}\in\mathcal{C}\left([0,T];P\right).$$

Proof: See the appendix.

5 Spectral Decomposition of the 3-D Problem

Now we are going to explain a hybrid method, which we have used for numerical computations. We split 3-D domain Ω to a 2-D vertical domain (x, z) perpendicular to the fault and the remaining 1D horizontal dimension along the fault plane marked by y.

A finite element method in the 2-D area and a Fourier transform decomposition in the third dimension are used. We can use the Fourier transform with respect to the coordinate y because the material parameter depend only on depth and moreover, there is no discontinuity in this horizontal direction.

Fourier Transform

We cannot use a Fourier decomposition in the depth dimension z, because of depth-dependance of material parameters. In horizontal direction x, perpendicular to the fault, the discontinuity of displacement will appear. Thus for the decomposition we choose the direction along the fault plane, which is denoted by y.

$$\widehat{\boldsymbol{v}}(x, k_y, z)\frac{1}{\sqrt{2\pi}}\int_{-\infty}^{\infty}\boldsymbol{v}(x, y, z)e^{-ik_y y}\,\mathrm{d}y. \tag{5.1}$$

We are transforming the real 3-D problem into the problem of searching for Fourier images in the 2-D domain. Afterwards we find this images for different coefficients k_y, we will use the inverse Fourier transform to obtain 3-D functions.

$$\boldsymbol{v}(x, y, z) = \frac{1}{\sqrt{2\pi}}\int_{-\infty}^{\infty}\widehat{\boldsymbol{v}}(x, k_y, z)e^{ik_y y}\,\mathrm{d}k_y \tag{5.2}$$

Elastic Problem

We transform now the equations (3.1) to their Fourier image and then derive the weak formulation. We substitute for τ to this equation of motion from Hooke's law.

$$\nabla\cdot[\lambda(\nabla\cdot\boldsymbol{u})\boldsymbol{I} + 2\mu\,\boldsymbol{\varepsilon}(\boldsymbol{u})]+\rho_0\,[(\nabla\cdot\boldsymbol{u})g_0\boldsymbol{e}_z - \nabla(g_0\boldsymbol{e}_z\cdot\boldsymbol{u})] = 0 \qquad \text{in } \Omega. \tag{5.3}$$

In the Fourier domain we get

$$\partial_x \left[\lambda \left(\partial_x \widehat{u}_x + ik_y \widehat{u}_y + \partial_z \widehat{u}_z\right) + \mu \partial_x \widehat{u}_x\right] + \mu \left(ik_y \partial_x \widehat{u}_y - k_y^2 \widehat{u}_x\right) + \partial_z \left[\mu \left(\partial_x \widehat{u}_z + \partial_z \widehat{u}_x\right)\right] - \rho_0 g_0 \partial_x \widehat{u}_z = 0 \tag{5.4}$$

$$\lambda \left(ik_y \partial_x \widehat{u}_x - k_y^2 \widehat{u}_y + ik_y \partial_z \widehat{u}_z\right) - 2\mu k_y^2 \widehat{u}_y + \partial_x \left[\mu \left(ik_y \widehat{u}_x + \partial_x \widehat{u}_y\right)\right] + \partial_z \left[\mu \left(ik_y \widehat{u}_z + \partial_z \widehat{u}_y\right)\right] - \rho_0 g_0 ik_y \widehat{u}_z = 0 \tag{5.5}$$

$$\partial_z \left[\lambda \left(\partial_x \widehat{u}_x + ik_y \widehat{u}_y + \partial_z \widehat{u}_z\right) + \mu \partial_z \widehat{u}_z\right] + \partial_x \left[\mu \left(\partial_z \widehat{u}_x + \partial_x \widehat{u}_z\right)\right] + \mu \left(ik_y \partial_z \widehat{u}_y - k_y^2 \widehat{u}_z\right) + \rho_0 g_0 \left(\partial_x \widehat{u}_x + ik_y \widehat{u}_y\right) - \rho_0 \partial_z g_0 \widehat{u}_z = 0. \tag{5.6}$$

To derive the weak formulation of these equations, we multiply them by a test function, integrate over 2-D domain and finally integrate by parts:

$$-\int_{\Omega_{2D}} \left\{\left[\lambda \left(\partial_x \widehat{u}_x + ik_y \widehat{u}_y + \partial_z \widehat{u}_z\right) + \mu \partial_x \widehat{u}_x\right] \partial_x \widehat{U}_x + \mu \left(\partial_x \widehat{u}_z + \partial_z \widehat{u}_x\right) \partial_z \widehat{U}_x\right\} \mathrm{d}x + \int_{\Omega_{2D}} \left[\mu \left(ik_y \partial_x \widehat{u}_y - k_y^2 \widehat{u}_x\right) - \rho_0 g_0 \partial_x \widehat{u}_z\right] \widehat{U}_x \, \mathrm{d}x = 0 \tag{5.7}$$

$$-\int_{\Omega_{2D}} \left\{\mu \left(ik_y \widehat{u}_x + \partial_x \widehat{u}_y\right) \partial_x \widehat{U}_y + \mu \left(ik_y \widehat{u}_z + \partial_z \widehat{u}_y\right) \partial_z \widehat{U}_y\right\} \mathrm{d}x + \int_{\Omega_{2D}} \left[\lambda \left(ik_y \partial_x \widehat{u}_x - k_y^2 \widehat{u}_y + ik_y \partial_z \widehat{u}_z\right) - 2\mu k_y^2 \widehat{u}_y - \rho_0 g_0 ik_y \widehat{u}_z\right] \widehat{U}_y \, \mathrm{d}x = 0 \tag{5.8}$$

$$-\int_{\Omega_{2D}} \left\{\mu \left(\partial_z \widehat{u}_x + \partial_x \widehat{u}_z\right) \partial_x \widehat{U}_z + \left[\lambda \left(\partial_x \widehat{u}_x + ik_y \widehat{u}_y + \partial_z \widehat{u}_z\right) + \mu \partial_z \widehat{u}_z\right] \partial_z \widehat{U}_z\right\} \mathrm{d}x + \int_{\Omega_{2D}} \left[\mu \left(ik_y \partial_z \widehat{u}_y - k_y^2 \widehat{u}_z\right) + \rho_0 g_0 \left(\partial_x \widehat{u}_x + ik_y \widehat{u}_y\right) - \rho_0 \partial_z g_0 \widehat{u}_z\right] \widehat{U}_z \, \mathrm{d}x = 0, \tag{5.9}$$

where $\widehat{U}_i$ are test functions independent upon y. Now we have 2-D problem, where k_y appears only as a parameter.

The displacement will be split in same way as was shown in the previous section $\widehat{\boldsymbol{u}} = \widehat{\overline{\boldsymbol{u}}} + \widehat{\boldsymbol{f}}$.

Viscoelastic Problem

For this problem it is possible to use the same Fourier transform as in the elastic case and except the number of unknowns the derivation is very similar.

6 Numerical method

Figure 5 shows a float chart which describes our numerical process.

Slip function

This section deals with numerical realization of the slip function $\boldsymbol{f}$, which will be used in our benchmarks and test cases. The function describe displacement on a fault and, simultaneously, it has to be defined to be continuous on some support domain with non-zero measure.

2-D Case

First, we introduce a mapping which will transform domain Ω_f to plain-coordinate support of an afterward defined function. This mapping is supposed to contain an inclination under specific angle, resize of dimensions and also shift of zero coordinations.

The parameters of the mapping are (see Figure 2)

- x_0 ... x-coordinate of the center of the fault on domain Ω
- z_0 ... depth of the center of the fault from surface of Earth
- d_1 ... half of the length of the fault
- d_2 ... width of the domain Ω_f, where the function $\boldsymbol{f}$ is defined
- o_a ... size of the outside part of the slip function $\boldsymbol{f}_\Gamma$, where the function f is continuously changing its value from 0 to 1
- o_b ... the second size of outside part of the slip function $\boldsymbol{f}$
- M ... the amplitude of the slip function
- α ... angle of the fault inclination to x-coordination, i.e. the dip angle

The mapping $P : (x, z) \to (p_1, p_2)$ is now defined as follows

$$\begin{aligned} p_1 &= \frac{1}{d_1}\left[+\cos\alpha(x - x_0) - \sin\alpha(z - z_0)\right] \\ p_2 &= \frac{1}{d_2}\left[-\sin\alpha(x - x_0) - \cos\alpha(z - z_0)\right] \end{aligned} \tag{6.1}$$

We have previously we introduced the main function $\boldsymbol{f}$, let us define the auxiliary function

$$o = o_a + p_2(o_b - o_a), \tag{6.2}$$

which expresses the size of outside borders, where the slip will be smoothed by the function $\cos^2$.

The scalar function (see Figure 3) describing the shape of the fault is defined as follows

$$f(x,z) \equiv \begin{cases} 0 & (|p_1| > 1) \\ & \vee\, (p_2 \notin (0,1)) \\ \cos^2\left(\frac{\pi}{2} p_2\right) & (|p_1| < 1 - \frac{o}{d_1}) \\ & \wedge\, (0 < p_2 < 1) \\ \cos^2\left(\frac{\pi}{2} p_2\right) \cos^2\left(\frac{\pi}{2} \frac{(|p_1|-1)d_1 + o}{o}\right) & (|p_1| > 1 - \frac{o}{d_1}) \\ & \wedge\, (|p_1| < 1) \\ & \wedge\, (0 < p_2 < 1). \end{cases} \tag{6.3}$$

To get the vector function $\boldsymbol{f}$, which gives the direction of the faulting we will multiply the scalar function f by tangential vector $\boldsymbol{t} = (\cos\alpha, -\sin\alpha)$. Apart that we also add the amplitude M

$$\boldsymbol{f} = M\ f\ \boldsymbol{t}. \tag{6.4}$$

3-D Case

In a real 3-D case we add following parameters.

- y_0 ... y-coordinate of the center of the fault on domain Ω
- d_3 ... half length of the fault along y-coordinate
- o_{3a} ... size of the outside part of the slip function $\boldsymbol{f}_\Gamma$ along y-coordinate, where the function f is continuously changing its value 0 to 1
- o_{3b} ... size of the outside part analogically as in case of o_b
- β ... angle of the fault inclination to the y-coordinate, i.e. the rake angle, see Figure 4.

Now we use the same scalar function as in the 2-D case in the coordinates (x, z) and denote it as f_{2D}. In the third coordinate y, we are going to define the 3-D function by a similar way as it was done in the case of the 2-D function in coordinate p_1.

$$f(x,y,z) \equiv \begin{cases} 0 & |y-y_0| > d_3 \\ f_{2D}(x,z) & |y-y_0| < d_3 - o_3 \\ f_{2D}(x,z)\cos^2\left(\dfrac{\pi}{2}\dfrac{|y-y_0|-d_3+o_3}{o_3}\right) & d_3-o_3 < |y-y_0| < d_3, \end{cases} \tag{6.5}$$

where $o_3 = o_{3a} + p_2(o_{3b} - o_{3a})$ is a function defined analogously as function o in the 2-D case. When we transform above function base to the Fourier domain, we obtain

$$\widehat{f}(x,k_y,z)\frac{f_{2D}(x,z)\sqrt{2}\pi^{\frac{3}{2}}}{(\pi^2 - k_y^2 o_3^2)k_y}\sin\left[\frac{k_y(2d_3-o_3)}{2}\right]\cos\left(\frac{k_y o_3}{2}\right)\left[\cos(k_y y_0) - i\sin(k_y y_0)\right]. \tag{6.6}$$

This scalar function is again multiplied by an amplitude M and tangential vector $\boldsymbol{t} = (\cos\alpha\sin\beta, \cos\beta, -\sin\alpha\sin\beta)$ which gives us the direction of the faulting as

$$\widehat{\boldsymbol{f}} = M\ \widehat{f}\ \boldsymbol{t}. \tag{6.7}$$

Finite Element Method

The computation mesh has been adapted according to the particular fault inclination, as you can see in Figure 6(a). We have thus used also the trapezoid elements except the standard oblong elements. Further, we have adjusted the size of elements according to the distance from the fault in order to get the best resolution of the fault.

The domain Ω is covered by a set of elements $\mathcal{T}_h$. Let us denote B_1, B_2 the sets of nodes which are lying on the boundary portions Γ_1, Γ_2 respectively. Then we can define finite element spaces

$$\begin{aligned} V_h &\equiv \left\{\boldsymbol{v} \in [\mathcal{C}(\Omega)]^2 ; v_i\big|_K \in Q_1(K)\ \forall K \in \mathcal{T}_h, i = x,z; \boldsymbol{v}(N) = 0\ \forall N \in B_2\right\} \\ P_h &\equiv \left\{\boldsymbol{p} \in \left[L^2(\Omega)\right]^3 ; p_i\big|_K = \text{ const. } \forall K \in \mathcal{T}_h, i = xx, xz, zz\right\}, \end{aligned} \tag{6.8}$$

i.e continuous bilinear elements are used for the displacement field and discontinuous constant elements for the stresses $\boldsymbol{\tau}$ and $\boldsymbol{\sigma}$. The dimensions are presented only for the 2-D case. In three dimensions we have not only more coordinates but also complex functions because of the Fourier transform. It means that dimensions for 3-D case are 6 and 12.

Figure 6(b) shows the degrees of freedom of the used elements. We note that even when we increased a number of degrees of freedom (e.g. quadratic

elements), the results were not significantly improved, which gave us a good argument to use rather a higher number of linear elements.

Time Discretization

In the case of viscoelastic problem we deal with the equations, where the time derivatives appear and except the spatial discretization we also need to deal with the numerical time scale. The equations are in the form

$$\partial_t A(x,t) + B(x,t) = 0. \tag{6.9}$$

We have used Crank-Nicolson scheme and got

$$\frac{A(x,t_{i+1}) - A(x,t_i)}{\Delta t} + \frac{B(x,t_{i+1}) + B(x,t_i)}{2} = 0. \tag{6.10}$$

Particularly, the equation describing the Maxwell rheology yields the form

$$\frac{\boldsymbol{\sigma}^{i+1} - \boldsymbol{\sigma}^i}{\Delta t} + \frac{\mu}{2\eta}(\boldsymbol{\sigma}^{i+1} + \boldsymbol{\sigma}^i) + \frac{\mu^2}{\eta}\left[\boldsymbol{\varepsilon}(\boldsymbol{u}^{i+1} + \boldsymbol{u}^i) - \frac{1}{3}\nabla\cdot(\boldsymbol{u}^{i+1} + \boldsymbol{u}^i)\boldsymbol{I}\right] = 0. \tag{6.11}$$

Stability of this scheme does not rely on the step length, i.e. the chosen scheme is unconditionally stable.

Practical Implementation

The numerical simulations were performed by means of the modified 2-D finite element code, originally Navier-Stokes equation solver programmed by Jaroslav Hron during his PhD work (Hron and Turek, 2005). We added mainly the Fourier transform, the 3-D mesh generator and the PREM model, see Dziewonski and Anderson (1981). The GMRES method with ILU preconditioning was used as a linear solver (Bramley and Wang, 1997).

7 Geophysical Models

In this section we present both 2-D and 3-D benchmarks.

2-D Benchmark

The first example is taken from Teisseyre (1986), which was employed as the 2-D benchmark of our method. The geometry of a domain is shown in Figure 7(a). In this example, we used constant Lamé coefficients and the

equation did not contain the pre-stressed force and the self-gravitation term. For this example we used a special slip function $\boldsymbol{f}$, which is composed from function defined in the above mentioned work Teisseyre (1986) and supplied by function $\cos^2$ as follows,

$$f(p1, p_2, q) \equiv \cos^2\left(\frac{\pi}{2}p_2\right) \times \begin{cases} \dfrac{3q - 1 + p_1}{2q^3}(1 - p_1)^2 & (1 - p_1) \leq 2q \\ \dfrac{-p_1^3 + 3p_1 + 2 - 3q(p_1 + 1)^2}{2(1 - q)^3} & (1 - p_1) > 2q, \end{cases} \tag{7.1}$$

for $p_1 \in [-1, 1]$, $p_2 \in [0, 1]$ and $q \in (0, 1)$. The plots of the functions for the coefficients $q = 0.3$, 0.5 and 0.7 are presented in Figure 7(b).

As Figure 8 shows, our results are almost identical with the results presented in Teisseyre (1986). Figure 9 shows the plots of vertical displacement on the whole domain Ω. Note that the computation was done on the mesh with 55,250 elements and 209,010 degrees of freedom.

1923 Kanto Earthquake

This model is again from Teisseyre (1986), where comparison of the numerical results with the real observed values for this Japanese earthquake (magnitude $M_S = 8.2$) was presented. Here we consider a fault in 3-D domain (see Figure 10) and also the equation of motion contains the pre-stressed force and the self-gravitation term. The equation coefficients (density, Lamé coefficients, gravitation acceleration) are computed from the PREM model.

The fault parameters: $x_0 = 0$, $y_0 = 0$, $z_0 = 13.75$ km, $d_1 = 27.5$ km, $d_2 = 10$ km, $d_3 = 42.5$ km, $o_a = 0$, $o_b = 10$ km, $o_{3a} = 2$ km, $o_{3b} = 10$ km, $M = 6.71$ m, $\alpha = 30°$ and $\beta = 153.44°$.

Since this problem is three-dimensional and the equations contain 18 unknowns, we have used the FEM on 2-D mesh with 2,400 elements and 35,118 degrees of freedom. The final 3-D mesh then contains 470,400 elements.

The results of our method are shown in Figures 11 and 12. These figures also show the results from Teisseyre (1986) and observed displacements. The model from the book used slightly different Lamé coefficients than our PREM values. Nevertheless, an agreement with our results is satisfying.

Note that in the model presented in Teisseyre (1986) a uniform slip on the whole fault is used. However, we changed a little bit our slip function by non-zero parameter o_{3a} in order to avoid the inaccuracy, which could arise from the spectral transform of such a discontinuous function.

Viscoelastic 2-D test

Now we turn our attention to the problem with the Maxwell rheology describing time relaxation of displacement and stress. This benchmark is again inspired by the book Teisseyre (1986). The assumed model of the Earth consists of an elastic plate of thickness 120 km overlying a viscoelastic layer. The behavior of lithosphere (elastic plate) is described by the Hooke's law and for the asthenosphere (viscoelastic layer) the Maxwell rheology is used. Analyzing the equations of the mentioned rheologies we can notice that the case involving the Hooke's law is actually the limit of Maxwell rheology when we put viscosity $\eta \to \infty$. From this point of view we can say that the interface between the layers causes only changes in the coefficients of the equation.

The calculation was performed for the three different faults:

(a) placed between the Earth's surface and the depth 90 km,

(b) connected fault situated from the depth 90 km to the asthenosphere,

(c) going through the whole lithosphere, i.e. (a)+(b).

The faults are displayed in Figure 13.

We chose viscosity $\eta = 10^{22} Pa \cdot s$ for the asthenosphere layer. From this value also the Maxwell time $\tau = 2\eta/\mu = 23.8$ kyr is determined, which represents the characteristic relaxation time.

The computing mesh contained 7,950 elements with 40,158 degrees of freedom.

Let us comment in detail the comparison of our results with the solution from Teisseyre (1986) in this viscoelastic model. As it is shown in Figure 14, there are substantial differences in the cases (a) and (c). The reason, why the results in the case (b) are in good agreement is that the active part of the fault is not reaching the surface of the Earth. The problems with faults which intersect the surface of the Earth are connected with the basic assumptions of our method. It is not possible to create displacement, which has discontinuity on the boundary Γ_1, where we have the boundary condition $\boldsymbol{\tau} \cdot \boldsymbol{n} = 0$. This condition is contained directly in the weak formulation and fixes the values at boundary points. This inaccuracy is already present in the elastic displacement in time $t = 0$, where on the left side from the fault the values are not fitting the exact solution. This exerts, after substraction of much higher values of elastic displacement, surely important effect on the viscoelastic relaxation. Note that these inaccuracies were already slightly appearing in our model of Kanto earthquake. However, with regard to the fact that we computed only elastic displacements in that case, it was not significantly obvious.

Coulomb Stress

When we try to predict how large is the impact exerted by previously broken fault to some near inactivated fault, we need to compute the incremental Coulomb stress. Basically we compute distribution of incremental stress around the first fault and recompute this values to a second potentially dangerous fault. The formula for incremental Coulomb stress is

$$\Delta CFF = \Delta\tau + \mu'\Delta\sigma, \tag{7.2}$$

where $\Delta\tau = \boldsymbol{t}\cdot\boldsymbol{\tau}\cdot\boldsymbol{n}$ is the shear stress change, $\Delta\sigma = \boldsymbol{n}\cdot\boldsymbol{\tau}\cdot\boldsymbol{n}$ is the normal stress change, $\boldsymbol{n}$ and $\boldsymbol{t}$ are the normal and tangent vectors to fault under interest and μ' is the coefficient of friction usually chosen to be around 0.6.

In Figure 15 the stresses, when the normal and tangent vectors of the inactivated fault are the same as those of the broken fault, are presented. We obtained the results, which are shown in Figure 16. Furthermore, we have added a plot showing isosurfaces of constant Coulomb stress.

The particular parameters of the slip function $\boldsymbol{f}$ are: $x_0 = 0$, $y_0 = 0$, $z_0 = 7.5$ km, $d_1 = 5$ km, $d_2 = 5$ km, $d_3 = 8$ km, $o_a = 0$, $o_b = 5$ km, $o_{3a} = 0.1$ km, $o_{3b} = 8$ km, $M = 0.6$ m, $\alpha = 90°$ and $\beta = 180°$.

We chose the parameters of the Fourier decomposition with regards to steep part of function $\boldsymbol{f}$ as $k_{step} = 0.0158$ and $n = 1600$. However, even though we have used relatively large number of Fourier coefficients, there are still visible small inaccuracies.

The 2-D mesh contains 1,820 elements with 33,342 degrees of freedom. The final 3-D mesh then contain 1,019,200 elements.

Lefkada and Cephalonia Earthquakes - influence of source inversion and topography effect

The earthquake from 14th August 2003 on the Lefkada island in Greece will be now used to demonstrate the Coulomb stress computations in a real simulation. The data were firstly presented in Karakostas et al. (2004). We have used the PREM model for densities and Lamé coefficients.

The fault parameters are: $x_0 = 0$, $y_0 = 0$, $z_0 = 7.5$ km, $d_1 = 5.196$ km, $d_2 = 5$ km, $d_3 = 8$ km, $o_a = 0$, $o_b = 5$ km , $o_{3a} = 0.1$ km, $o_{3b} = 8$ km, $M = 0.6$ m, $\alpha = 60°$ and $\beta = -175°$.

The parameters of the Fourier decomposition are $k_{step} = 0.0632$, $n = 800$.

The complete orientation of the Lefkada fault is (18°, 60°, −175°), where the angles denote (strike, dip, rake). The Coulomb stress is computed for the orientation of the Cephalonia fault (28°, 82°, 172°), which the center point locate in $x_1 = -1.31$ km, $y_1 = -37.47$ km. The results obtained by our model can be compared with the results from Karakostas (2004) in Figure 17.

An alternative analysis by Zahradník et al. (2005) found that there were at least two separated sources of the observed earthquake. According to the analysis, the orientation of the Lefkada fault was (17°, 88°, −177°), the size of the fault plate is 18 km x 9 km and the slip amplitude was $|\boldsymbol{f}| = 0.6$ m. The orientation of Cephalonia fault was (24°, 74°, 164°), the sizes were 15 km x 7.5 km, and $|\boldsymbol{f}| = 0.9$ m. Note that our calculation should represent only an attempt to calculate stress changes produced by such a two-source event. The problem is that our method is not able to cover the situation when the two faults have different inclinations in y-axis. In this particular example we omit the 7 degree dip angle difference and we consider the faults to be placed in the same plane with their centers to be distant $37,5$ km.

The parameters of the fault $\boldsymbol{f}_1$ are: $x_0 = 0$, $y_0 = 18.75$ km, $z_0 = 7.5$ km, $d_1 = 4.5$ km, $d_2 = 5$ km, $d_3 = 9$ km, $o_a = 0$, $o_b = 4.5$ km, $o_{3a} = 0.1$ km, $o_{3b} = 9$ km, $M = 0.6$ m, $\alpha = 88°$ and $\beta = -177°$.

The parameters of the fault $\boldsymbol{f}_2$ are: $x_0 = 0$, $y_0 = -18.75$ km, $z_0 = 7.5$ km, $d_1 = 3.75$ km, $d_2 = 5$ km, $d_3 = 7.5$ km, $o_a = 0$, $o_b = 3.75$ km, $o_{3a} = 0.1$ km, $o_{3b} = 7.5$ km, $M = 0.9$ m, $\alpha = 74°$ and $\beta = 164°$.

The parameters of the Fourier decomposition are $k_{step} = 0.0316$, $n = 800$.

We calculate the Coulomb stress for the plane with the orientation (20.5°, 81°, 173.5°), which is as an average value of angles of both active fault planes.

We can see from the plots in Figure 18 that the place with the highest increment of the Coulomb stress is between the faults, where is thus potentially the highest risk of further earthquake. However, we do not know the stresses which were accumulated in this area before the 2004 earthquake, and

thus we are not able to speculate about the whole stress.

We chose the dimensions of the computation domain to be 120 km x 120 km x 30 km in both interpretations. The 2-D mesh contained 1,820 elements with 33,342 degrees of freedom in both computations. The final 3-D mesh thus contained 1,019,200 elements.

Finally we present how a topography of the surface can influence the results. Application of FEM allows us to change the elevation of the surface along the x direction, and thus to incorporate a topography slope of the Mediterranean area around the Greek islands. To obtain an approximation of real topography effects we recalculate the one-event interpretation of the Lefkada earthquake with 3 km decrease of the topography on the sea side and 1 km increase on the continental side. Figure 19 shows x, y, z displacements and the Coulomb stress for (a) flat surface, (b) "real" topography and (c) differences of both results. The differences are distinctive, up to 30% in case of displacements and up to 33% in case of Coulomb stress.

There are ambiguities in seismic source inverse problems. An example is the interpretation of the 2003 Lefkada earthquake where it is hard to resolve between one-event and double-event interpretations obtained from the Greek seismic network data. However, our simulations show that the stress distributions are substantially different. Moreover, the topological effect is also non-negligible. Further progress in both seismic source modelling and coseismic response computations including real topographies are thus needed to obtain more reliable estimates of seismic hazard by means of the Coulomb stress calculations.

8 Concluding Remarks

It is obvious that there are high computer memory and time requirements if 3-D FEM is applied to problems, where high resolution is needed. On the other hand, we need not take into account structural changes in a horizontal direction along the fault in many common problems. Such problems can be thus decoupled in the spectral domain corresponding to this direction. We have demonstrated that the corresponding spectral - finite element method is than efficient for both coseismic and postseismic relaxation computations.

The efficiency of this approach becomes more substantial when time-dependent problems of postseismic relaxation are solved, an example of such a modelling is given in Figure 14. Note that viscoelastic phenomena are important especially for buried faults where singular magnitudes of the stress can be obtained at the places of abrupt slip changes on a fault.

If we add the inertial term into the equation of motion, we obtain hyper-

bolic equation, which represents wave propagation. However, wave propagation simulations require to significantly shorten the time step in the temporal discretizations. We are in principle able to get also the wave propagation, however, there are lots of complicated numerical aspects, e.g. the energy conservation, mesh resolution, non-reflective boundary conditions and so on.

Further work is needed to extend our approach, e.g., for simulation of the so-called tsunamigenic seafloor deformation. To create a model of this coupled tsunami-seismogenic problem it will be necessary to adapt our method for seismic wave propagation in a 3-D domain with a thin uppermost water layer and then in the second step to compute a shallow water equation problem over the 2-D surface domain. The sea floor depth $\eta(x, y, t)$ taken from the 3-D model would serve as the source term in the water equation.

Acknowledgments

We are grateful to Dave A. Yuen for his comments support and encouragement, Milan Pokorný for his help with proving mathematical theorems, Jaroslav Hron for providing us with his 2-D FEM code, Libor Inovecký for long discussions and two anonymous reviewers for their constructive comments. The output of 2-D and 3-D results were visualized by using the freely available GMV software, see http://www-xdiv.lanl.gov/XCM/gmv/GMVHome.html. This research was supported by the Czech National Foundation under the grant No. 205/03/0778 and by the research project MSM 0021620800 of the Czech Ministry of Education.

A Appendix

Both proofs provided below are done in a similar way as one can find in Inovecký (2003).

Proof: **[Existence and Uniqueness of the Elastic Problem]**
We are going to provide the proof for the weak formulation (4.4). From the Lax-Milgram theorem, see Nečas and Hlaváček (1981), we prove the existence for $\overline{\boldsymbol{u}}$, which will be uniqueness for chosen function $\boldsymbol{f}$. Further we add a proof of the claim that function $\boldsymbol{u}$ is not depend on this arbitrary slip function $\boldsymbol{f}$ and it is thus uniqueness for a prescribed $\boldsymbol{f}_\Gamma$.

For the Lax-Milgram theorem to be applied, we need to show boundedness and ellipticity of bilinear forms and also the boundedness of the r.h.s. From basic inequalities we get

$$\|\nabla \cdot \boldsymbol{U}\|_2^2 \leq 3\,\|\nabla \boldsymbol{U}\|_2^2\,, \quad \|\boldsymbol{\varepsilon}(\boldsymbol{U})\|_2 \leq \|\nabla \boldsymbol{U}\|_2 \qquad \forall \boldsymbol{U} \in V \tag{A.1}$$

and from Hölder inequality we obtain boundedness of the forms $a(\cdot,\cdot)$ and $b(\cdot,\cdot)$

$$|a\,(\boldsymbol{U},\boldsymbol{V})| \leq (2\,\|\mu\|_\infty + 3\,\|\lambda\|_\infty)\,\|\boldsymbol{U}\|_V\,\|\boldsymbol{V}\|_V =: \|a\|\,\|\boldsymbol{U}\|_V\,\|\boldsymbol{V}\|_V \tag{A.2a}$$

$$|b\,(\boldsymbol{U},\boldsymbol{V})| \leq (1+\sqrt{3})\,\|\rho_0\|_\infty\,\|g_0\|_{1,\infty}\,\|\boldsymbol{U}\|_V\,\|\boldsymbol{V}\|_2 =: \|b\|\,\|\boldsymbol{U}\|_V\,\|\boldsymbol{V}\|_2\,, \tag{A.2b}$$

where we defined $\|a\|$ and $\|b\|$ to be linear combinations of the coefficient norms.

We get the boundedness of the r.h.s. by using of the trace theorem and the boundedness of the forms $a(\cdot,\cdot)$ and $b(\cdot,\cdot)$:

$$F_1(\boldsymbol{U}) \leq (\|a\| + \|b\|)\,\|\boldsymbol{f}\|_{1,2,\Omega_f}\,\|\boldsymbol{U}\|_V\,. \tag{A.3}$$

To prove V-ellipticity of bilinear form $a(\cdot,\cdot)$ we use the following lemma, see Nečas and Hlaváček (1981).

Lemma A.1 (Korn's inequality)
Let $\boldsymbol{U} \in V \equiv \left\{\boldsymbol{v} \in [W^{1,2}(\Omega)]^3\,; \boldsymbol{v}\big|_{\Gamma_2} = 0\right\}$*, where subset* Γ_2 *is non-empty, open with respect to* $\partial\Omega$*. Then there exists constant* C_K *(dependant on* Ω *and* Γ_2*) that this holds*

$$\int_\Omega \boldsymbol{\varepsilon}(\boldsymbol{U}) : \boldsymbol{\varepsilon}(\boldsymbol{U})\;\mathrm{d}x \geq C_K\,\|\boldsymbol{U}\|_V^2\,. \tag{A.4}$$

Under the assumption that the Lamé coefficients obey the inequalities

$$0 \leq \lambda(\boldsymbol{x}), \quad 0 < \mu_0 \leq \mu(\boldsymbol{x}) \qquad \text{a.e. in } \Omega, \tag{A.5}$$

the bilinear form $a(\cdot,\cdot)$ fulfills

$$a\left(\boldsymbol{U},\boldsymbol{U}\right) = \int_\Omega 2\mu\, \boldsymbol{\varepsilon}(\boldsymbol{U}) : \boldsymbol{\varepsilon}(\boldsymbol{U})\, \mathrm{d}x + \int_\Omega \lambda |\nabla\cdot\boldsymbol{U}|^2\, \mathrm{d}x \geq 2\mu_0 \int_\Omega \boldsymbol{\varepsilon}(\boldsymbol{U}) : \boldsymbol{\varepsilon}(\boldsymbol{U})\, \mathrm{d}x, \tag{A.6}$$

or

$$a\left(\boldsymbol{U},\boldsymbol{U}\right) \geq 2\mu_0 C_K \left\|\boldsymbol{U}\right\|_V^2 \qquad \forall \boldsymbol{U} \in V. \tag{A.7}$$

From this V-ellipticity of the bilinear form $a(\cdot,\cdot)$ and the boundedness of the bilinear form $b(\cdot,\cdot)$, we get V-ellipticity of the whole l.h.s. of (4.4), if the condition

$$0 < C_{ab} := 2\mu_0 C_K - (1+\sqrt{3})\left\|\rho_0\right\|_\infty \left\|g_0\right\|_{1,\infty} \tag{A.8}$$

is satisfied.

Now we can use the Lax-Milgram theorem and we have thus existence of one $\overline{\boldsymbol{u}}$ for any chosen $\boldsymbol{f}$. We prove uniqueness of $\boldsymbol{u}$ in a following way: we choose two different slip functions $\boldsymbol{f}_1 \neq \boldsymbol{f}_2$ and show that if both of them have the same trace on Γ, then $\boldsymbol{u}_1 = \boldsymbol{u}_2$.

First, we subtract these two functions and denote their difference as $\boldsymbol{f}$, then we know that $T_\Gamma \boldsymbol{f} = 0$ and $\boldsymbol{f} \in V$. From the Lax-Milgram theorem we gain the existence of $\overline{\boldsymbol{u}}_1$ and $\overline{\boldsymbol{u}}_2$ and equation (4.4) thus yields

$$a\left(\overline{\boldsymbol{u}}_1 - \overline{\boldsymbol{u}}_2, \boldsymbol{U}\right) + b\left(\overline{\boldsymbol{u}}_1 - \overline{\boldsymbol{u}}_2, \boldsymbol{U}\right) = F_1(\boldsymbol{U}) \qquad \forall \boldsymbol{U} \in V, \tag{A.9}$$

where the function $\boldsymbol{f} \in V$ is in the form $F_1(\cdot)$. We can thus rewrite bilinear forms $a(\cdot,\cdot)$ and $b(\cdot,\cdot)$:

$$a\left(\overline{\boldsymbol{u}}_1 - \overline{\boldsymbol{u}}_2 + \boldsymbol{f}_1 - \boldsymbol{f}_2, \boldsymbol{U}\right) + b\left(\overline{\boldsymbol{u}}_1 - \overline{\boldsymbol{u}}_2 + \boldsymbol{f}_1 - \boldsymbol{f}_2, \boldsymbol{U}\right) = 0 \qquad \forall \boldsymbol{U} \in V. \tag{A.10}$$

This relation already shows

$$\overline{\boldsymbol{u}}_1 + \boldsymbol{f}_1 = \overline{\boldsymbol{u}}_2 + \boldsymbol{f}_2 \tag{A.11}$$

and thus $\boldsymbol{u}_1 = \boldsymbol{u}_2$. From Hooke's law we have also uniqueness of the stress $\boldsymbol{\tau}$.

Proof: **[Existence and Uniqueness of the Viscoelastic Problem]**

The formulation (4.6) shows that the first equation is time independent and thus we can make the estimate separately and then we will not need to consider it in the following steps.

The proof of existence and uniqueness for the second evolutional equation is done by the Galerkin method, see Evans (1998). First, the solution $\boldsymbol{\sigma}$ will be approximated on the finite dimensional subspace of the space P by the Galerkin approximations. Further, we will prove boundedness of the solution sequence in the proper Bochner space and then we will show that weak limit of this sequence is a solution $\overline{\boldsymbol{u}}$. Finally, we prove the uniqueness of the solution $\boldsymbol{u}$ and $\boldsymbol{\sigma}$, by means of the similar arguments as in the elastic case.

Step 1: Reduction of the number of unknowns
The argumentation used in the elastic case leads to fact that all the variables except $\boldsymbol{\sigma}$ can be eliminated from the system of equations, i.e., they can be explicitly express by variable $\boldsymbol{\sigma}$.

Let us adapt the equation of motion (4.6a)

$$a\left(\overline{\boldsymbol{u}}, \boldsymbol{U}\right) + b\left(\overline{\boldsymbol{u}}, \boldsymbol{U}\right) F_1(\boldsymbol{U}) - \left(\boldsymbol{\sigma}, \boldsymbol{\varepsilon}(\boldsymbol{U})\right)_P \qquad \forall \boldsymbol{U} \in V \tag{A.12}$$

and show that the whole r.h.s. is bounded, linear form on the space V. Namely, $F_1(\cdot)$ is bounded and we can also estimate the second term as follows,

$$\left|\left(\boldsymbol{\sigma}, \boldsymbol{\varepsilon}(\boldsymbol{U})\right)_P\right| \leq \|\boldsymbol{\sigma}\|_P \|U\|_V \qquad \forall \boldsymbol{U} \in V, \tag{A.13}$$

provided that $\boldsymbol{\sigma} \in P$.

As pointed out earlier, the bilinear form $a(\cdot,\cdot) + b(\cdot,\cdot)$ is bounded and elliptic. Therefore, due to the Lax-Milgram theorem, there exists a unique solution $\overline{\boldsymbol{u}}$ of equation (A.12). This solution is bounded by the r.h.s. terms through the inequality

$$\|\overline{\boldsymbol{u}}\|_V \leq \frac{1}{\sqrt{C_{ab}}} \left[\left(\|a\| + \|b\|\right) \|\boldsymbol{f}\|_{1,2,\Omega_f} + \|\boldsymbol{\sigma}\|_P \right], \tag{A.14}$$

where C_{ab} is the ellipticity constant of the bilinear form $a(\cdot,\cdot) + b(\cdot,\cdot)$.

Thus, for a fixed function $\boldsymbol{f}$, there exists a continues linear mapping $\mathcal{L}_{\boldsymbol{f}}$ such that

$$\mathcal{L}_{\boldsymbol{f}} : P \to V, \qquad \overline{\boldsymbol{u}} = \mathcal{L}_{\boldsymbol{f}} \boldsymbol{\sigma} \tag{A.15}$$

and $\overline{\boldsymbol{u}}$, $\boldsymbol{\sigma}$ fulfil equation (A.12).

Further, it is sufficent to deal only with equation (4.6b) for $\boldsymbol{\sigma}$, which is transformed after a substitution from (A.15) to

$$\left(\partial_t \boldsymbol{\sigma}, \boldsymbol{\mathcal{S}}\right)_P + \left(\frac{\mu}{\eta}\boldsymbol{\sigma}, \boldsymbol{\mathcal{S}}\right)_P + c\left(\mathcal{L}_{\boldsymbol{f}}\boldsymbol{\sigma}, \boldsymbol{\mathcal{S}}\right) = F_2(\boldsymbol{\mathcal{S}}) \qquad \forall \boldsymbol{\mathcal{S}} \in P, \tag{A.16}$$

plus the initial condition

$$\boldsymbol{\sigma}(\boldsymbol{x}, 0) = 0. \tag{A.17}$$

Step 2: Galerkin approximations

The space $P \subset [L^2(\Omega)]^{3\times 3}$ is separable, thus we can choose its basis:

$$\{\boldsymbol{\mathcal{S}}_k\}_{k=1}^{\infty} \subset P \tag{A.18}$$

and this basis may be constructed as orthonormal.

The Galerkin approximations are the solutions of the projection of the evolutionary problem (A.16), (A.17) onto a finite dimensional subspace $P_m \equiv \text{span}\{\boldsymbol{\mathcal{S}}_k\}_{k=1}^{m}$. Thus, they can be sought in the form

$$\boldsymbol{\sigma}_m(t) = \sum_{k=1}^{m} \alpha_m^k(t)\boldsymbol{\mathcal{S}}_k, \tag{A.19}$$

where $\boldsymbol{\sigma}_m : [0,T] \to P$ and $\alpha_m^k : [0,T] \to \mathcal{R},\ k = 1,...,m$. By substituting the approximate solution $\boldsymbol{\sigma}_m$ into the equation (A.16) and into the initial condition (A.17), we obtain the initial value problem

$$(\partial_t \boldsymbol{\sigma}_m, \boldsymbol{\mathcal{S}})_P + \left(\frac{\mu}{\eta}\boldsymbol{\sigma}_m, \boldsymbol{\mathcal{S}}\right)_P + c\left(\mathcal{L}_{\boldsymbol{f}}\boldsymbol{\sigma}_m, \boldsymbol{\mathcal{S}}\right) = F_2(\boldsymbol{\mathcal{S}}) \quad \forall \boldsymbol{\mathcal{S}} \in P_m \tag{A.20a}$$

$$(\boldsymbol{\sigma}_m(0), \boldsymbol{\mathcal{S}})_P = 0 \qquad \forall \boldsymbol{\mathcal{S}} \in P_m. \tag{A.20b}$$

Let us show that this finite dimensional problem admits a unique solution. By substituting from the definition (A.19), putting the basis functions $\boldsymbol{\mathcal{S}}_j$ as test functions and taking into account the orthonormality of the chosen basis, we can rewrite the preceding problem as

$$\frac{\mathrm{d}\alpha_m^j}{\mathrm{d}t} + \sum_{k=1}^{m} \alpha_m^k \left(\frac{\mu}{\eta}\boldsymbol{\mathcal{S}}_k, \boldsymbol{\mathcal{S}}_j\right)_P + \sum_{k=1}^{m} \alpha_m^k c\left(\mathcal{L}_{\boldsymbol{f}}\boldsymbol{\mathcal{S}}_k, \boldsymbol{\mathcal{S}}_j\right) = F_2(\boldsymbol{\mathcal{S}}_j) \qquad j = 1,...,m \tag{A.21a}$$

$$\alpha_m^j(0) = 0 \qquad j = 1,...,m. \tag{A.21b}$$

When we introduce the following notation

$$C_{jk} = \left(\frac{\mu}{\eta}\boldsymbol{\mathcal{S}}_k, \boldsymbol{\mathcal{S}}_j\right)_P, \qquad D_{jk} = c\left(\mathcal{L}_{\boldsymbol{f}}\boldsymbol{\mathcal{S}}_k, \boldsymbol{\mathcal{S}}_j\right), \qquad G_j = F_2(\boldsymbol{\mathcal{S}}_j), \tag{A.22}$$

we can rewrite the linear ODE system (A.21a) in the matrix form

$$\frac{\mathrm{d}\boldsymbol{\alpha}_m}{\mathrm{d}t} + \mathbb{C}\,\boldsymbol{\alpha}_m + \mathbb{D}\,\boldsymbol{\alpha}_m = \boldsymbol{G}. \tag{A.23}$$

The matrixes $\mathbb{C}$, $\mathbb{D}$ and vector $\boldsymbol{G}$ are time independent, which together with the standard ODE theory immediately imply the global existence and uniqueness of the $\mathcal{C}^1$ functions $\boldsymbol{\alpha}_m(t)(\alpha_m^1(t),\dots,\alpha_m^m(t))$, which fulfil equation (A.21). Simultaneously, we gain the existence and uniqueness of the solutions $\boldsymbol{\sigma}_m$ for the problem (A.20).

Step 3: Energetic estimates

Let us choose $\boldsymbol{\sigma}_m$ as the test function in equation (A.20a)

$$(\partial_t\boldsymbol{\sigma}_m,\boldsymbol{\sigma}_m)_P+\left(\frac{\mu}{\eta}\boldsymbol{\sigma}_m,\boldsymbol{\sigma}_m\right)_P+c\left(\mathcal{L}_{\boldsymbol{f}}\boldsymbol{\sigma}_m,\boldsymbol{\sigma}_m\right)=F_2(\boldsymbol{\sigma}_m). \tag{A.24}$$

Using Hölder's inequality and the inequalities

$$\|\operatorname{Tr}\boldsymbol{\mathcal{S}}\|_2^2\le 3\,\|\boldsymbol{\mathcal{S}}\|_2^2\quad\forall\boldsymbol{\mathcal{S}}\in P,\qquad \|\nabla\cdot\boldsymbol{U}\|_2^2\le 3\,\|\nabla\boldsymbol{U}\|_2^2\quad\forall\boldsymbol{U}\in V, \tag{A.25}$$

we show that the bilinear form $c(\cdot,\cdot)$ is bounded

$$c\left(\boldsymbol{U},\boldsymbol{\mathcal{S}}\right)\le 4\left\|\frac{\mu^2}{\eta}\right\|_\infty\|\boldsymbol{U}\|_V\,\|\boldsymbol{\mathcal{S}}\|_P\,, \tag{A.26}$$

especially

$$\begin{aligned}c\left(\mathcal{L}_{\boldsymbol{f}}\boldsymbol{\sigma}_m,\boldsymbol{\sigma}_m\right)&\le\frac{4}{\sqrt{C_{ab}}}\left\|\frac{\mu^2}{\eta}\right\|_\infty\left[(\|a\|+\|b\|)\,\|\boldsymbol{f}\|_{1,2,\Omega_f}+\|\boldsymbol{\sigma}_m\|_P\right]\|\boldsymbol{\sigma}_m\|_P\\&\le\frac{2}{\sqrt{C_{ab}}}\left\|\frac{\mu^2}{\eta}\right\|_\infty\left[3\,\|\boldsymbol{\sigma}_m\|_P^2+(\|a\|+\|b\|)^2\,\|\boldsymbol{f}\|_{1,2,\Omega_f}^2\right].\end{aligned} \tag{A.27}$$

Considering that

$$\frac{\mu(\boldsymbol{x})}{\eta(\boldsymbol{x})}\ge 0\quad\text{a.e. in }\Omega, \tag{A.28}$$

we can estimate

$$\left(\frac{\mu}{\eta}\boldsymbol{\sigma}_m,\boldsymbol{\sigma}_m\right)_P\ge 0. \tag{A.29}$$

And by making use of

$$(\partial_t\boldsymbol{\sigma}_m,\boldsymbol{\sigma}_m)_P=\frac{\mathrm{d}}{\mathrm{d}t}\left(\frac{1}{2}\,\|\boldsymbol{\sigma}_m\|_P^2\right), \tag{A.30}$$

we can use the estimates (A.27), (A.26) for the r.h.s. and the equation (A.24) to get the inequality

$$\frac{\mathrm{d}}{\mathrm{d}t}\,\|\boldsymbol{\sigma}_m\|_P^2\le 4\left\|\frac{\mu^2}{\eta}\right\|_\infty\left[\left(1+\frac{3}{\sqrt{C_{ab}}}\right)\|\boldsymbol{\sigma}_m\|_P^2+\left(1+\frac{(\|a\|+\|b\|)^2}{\sqrt{C_{ab}}}\right)\|\boldsymbol{f}\|_{1,2,\Omega_f}^2\right]. \tag{A.31}$$

Lemma A.2 (Gronwall) *Let $y(t), \alpha(t), \beta(t)$ be non-negative functions defined on $[0,T]$ such that*

$$\dot{y}(t) \leq \alpha(t)\ y(t) + \beta(t) \qquad \forall t \in (0,T). \tag{A.32}$$

Then

$$y(t) \leq e^{\int_0^t \alpha(s)\ \mathrm{d}s} \left[y(0) + \int_0^t \beta(s)\ \mathrm{d}s \right] \qquad \forall t \in (0,T). \tag{A.33}$$

In our case, this yields

$$\|\boldsymbol{\sigma}_m(t)\|_P^2 \leq e^{At} Bt\, \|\boldsymbol{f}\|_{1,2,\Omega_f}^2 \quad \forall t \in (0,T), \tag{A.34}$$

where constants A and B are defined as

$$A = 4 \left\| \frac{\mu^2}{\eta} \right\|_\infty \left(1 + \frac{3}{\sqrt{C_{ab}}} \right), \qquad B = 4 \left\| \frac{\mu^2}{\eta} \right\|_\infty \left(1 + \frac{(\|a\| + \|b\|)^2}{\sqrt{C_{ab}}} \right). \tag{A.35}$$

If we substitute T instead of t on the r.h.s. of the inequality (A.34), the value of the r.h.s. will not decrease, hence

$$\|\boldsymbol{\sigma}_m(t)\|_P^2 \leq e^{AT} BT\, \|\boldsymbol{f}\|_{1,2,\Omega_f}^2 \qquad \forall t \in (0,T). \tag{A.36}$$

Integrating this result with respect to the time t, we obtain that the Galerkin approximations $\boldsymbol{\sigma}_m$ lie and are uniformly bounded in the space

$$\boldsymbol{\sigma}_m \in L^\infty\left((0,T); P\right) \qquad \forall m \in \mathcal{N}. \tag{A.37}$$

Let us now derive, in which space the functions $\partial_t \boldsymbol{\sigma}_m$ lie. For this purpose we just test the equation (A.20) by the function $\partial_t \boldsymbol{\sigma}_m$

$$\|\partial_t \boldsymbol{\sigma}_m\|_P^2 + \left(\frac{\mu}{\eta} \boldsymbol{\sigma}_m, \partial_t \boldsymbol{\sigma}_m \right)_P + c\left(\mathcal{L}_{\boldsymbol{f}} \boldsymbol{\sigma}_m, \partial_t \boldsymbol{\sigma}_m \right) = F_2(\partial_t \boldsymbol{\sigma}_m). \tag{A.38}$$

From this formula, from inequality (A.26) and from the first part of estimate (A.27) we gain

$$\|\partial_t \boldsymbol{\sigma}_m\|_P \leq \left(\left\| \frac{\mu}{\eta} \right\|_\infty + \frac{4}{\sqrt{C_{ab}}} \left\| \frac{\mu^2}{\eta} \right\|_\infty \right) \|\boldsymbol{\sigma}_m\|_P + 4 \left\| \frac{\mu^2}{\eta} \right\|_\infty \left(1 + \frac{\|a\| + \|b\|}{\sqrt{C_{ab}}} \right) \|\boldsymbol{f}\|_{1,2,\Omega_f}. \tag{A.39}$$

If we use estimate (A.36) and integrate this inequality over the interval $[0,T]$, we gain

$$\int_0^T \|\partial_t \boldsymbol{\sigma}_m\|_P\ \mathrm{d}t \leq C\, \|\boldsymbol{f}\|_{1,2,\Omega_f}, \tag{A.40}$$

where C does not depend on m.

We have thusderived that approximations $\partial_t \boldsymbol{\sigma}_m$ are uniformly bounded in the space $L^\infty\left((0,T); P\right)$ for $\forall m \in \mathcal{N}$.

Step 4: Passing to a weak limit

To obtain a weak solution of the problem, we pass to a limit as $m \to \infty$. Since the sequence $\{\boldsymbol{\sigma}_m\}_{m=1}^{\infty}$ is bounded in the Bochner space $W^{1,\infty}((0,T);P)$, we can choose a weakly convergent subsequence $\boldsymbol{\sigma}_{m_l}$ such that

$$\boldsymbol{\sigma}_{m_l} \overset{*}{\rightharpoonup} \boldsymbol{\sigma} \qquad *\text{-weakly in } W^{1,\infty}((0,T);P)\,, \tag{A.41}$$

where $\boldsymbol{\sigma}$ denotes the corresponding weak limit. Now we keep a fixed integer N and a test function $\boldsymbol{\mathcal{V}} \in \mathcal{C}^1([0,T];P)$ as

$$\boldsymbol{\mathcal{V}}(t) = \sum_{k=1}^{N} \beta_k(t)\boldsymbol{\mathcal{S}}_k, \tag{A.42}$$

where β_k are given smooth functions. We put these test functions in place of $\boldsymbol{\mathcal{S}}$ in equation (A.20a) with $m \geq N$, and integrate the result over interval $[0,T]$

$$\int_0^T \left[(\partial_t\boldsymbol{\sigma}_m, \boldsymbol{\mathcal{V}})_P + \left(\frac{\mu}{\eta}\boldsymbol{\sigma}_m, \boldsymbol{\mathcal{V}}\right)_P + c\left(\mathcal{L}_{\boldsymbol{f}}\boldsymbol{\sigma}_m, \boldsymbol{\mathcal{V}}\right)\right] \mathrm{d}t \int_0^T F_2(\boldsymbol{\mathcal{V}})\ \mathrm{d}t. \tag{A.43}$$

By setting $m = m_l$ and then also by passing to the limit as $m_l \to \infty$ we gain

$$\int_0^T \left[(\partial_t\boldsymbol{\sigma}, \boldsymbol{\mathcal{V}})_P + \left(\frac{\mu}{\eta}\boldsymbol{\sigma}, \boldsymbol{\mathcal{V}}\right)_P + c\left(\mathcal{L}_{\boldsymbol{f}}\boldsymbol{\sigma}, \boldsymbol{\mathcal{V}}\right)\right] \mathrm{d}t = \int_0^T F_2(\boldsymbol{\mathcal{V}})\ \mathrm{d}t. \tag{A.44}$$

Because of the functions are dense in the considered Bochner space, this equality holds for all $\boldsymbol{\mathcal{V}} \in L^2((0,T);P)$. Therefore, we get

$$(\partial_t\boldsymbol{\sigma}, \boldsymbol{\mathcal{S}})_P + \left(\frac{\mu}{\eta}\boldsymbol{\sigma}, \boldsymbol{\mathcal{S}}\right)_P + c\left(\mathcal{L}_{\boldsymbol{f}}\boldsymbol{\sigma}, \boldsymbol{\mathcal{S}}\right) = F(\boldsymbol{\mathcal{S}}) \qquad \forall \boldsymbol{\mathcal{S}} \in P, \text{ for a.e. } t \in (0,T), \tag{A.45}$$

i.e. we found the weak solution $\boldsymbol{\sigma} \in W^{1,\infty}((0,T);P)$ of equation (A.16) and according to Evans (1998) it implies that $\boldsymbol{\sigma} \in \mathcal{C}([0,T];P)$ and, furthermore,

$$\max_{0\leq t\leq T} \|\boldsymbol{\sigma}(t)\|_P \leq C\,\|\boldsymbol{f}\|_{1,2,\Omega_f}\,, \tag{A.46}$$

which yields the uniqueness of the solution $\boldsymbol{\sigma}$ and $\overline{\boldsymbol{u}}$ for any chosen $\boldsymbol{f}$.

To confirm a fulfillment of the initial condition (A.17), we firstly choose a test function $\boldsymbol{\mathcal{V}} \in \mathcal{C}^1([0,T];P)$ with $\boldsymbol{\mathcal{V}}(T) = 0$ and using integration by parts in equation (A.44) we get

$$\int_0^T \left[-(\boldsymbol{\sigma}, \partial_t\boldsymbol{\mathcal{V}})_P + \left(\frac{\mu}{\eta}\boldsymbol{\sigma}, \boldsymbol{\mathcal{V}}\right)_P + c\left(\mathcal{L}_{\boldsymbol{f}}\boldsymbol{\sigma}, \boldsymbol{\mathcal{V}}\right)\right] \mathrm{d}t \int_0^T F_2(\boldsymbol{\mathcal{V}})\,\mathrm{d}t + (\boldsymbol{\sigma}(0), \boldsymbol{\mathcal{V}}(0))_P\,. \tag{A.47}$$

Similarly, it follows from the equation (A.43) that

$$\int_0^T \left[-\left(\boldsymbol{\sigma}_m, \partial_t \boldsymbol{\mathcal{V}}\right)_P + \left(\frac{\mu}{\eta}\boldsymbol{\sigma}_m, \boldsymbol{\mathcal{V}}\right)_P + c\left(\mathcal{L}_{\boldsymbol{f}}\boldsymbol{\sigma}_m, \boldsymbol{\mathcal{V}}\right) \right] \mathrm{d}t = \int_0^T F_2(\boldsymbol{\mathcal{V}})\ \mathrm{d}t + \left(\boldsymbol{\sigma}_m(0), \boldsymbol{\mathcal{V}}(0)\right)_P . \tag{A.48}$$

On the other hand, if we choose $m = m_l$, we can use a weak limit of $\boldsymbol{\sigma}_m$, as in (A.41), to obtain

$$\int_0^T \left[-\left(\boldsymbol{\sigma}, \partial_t \boldsymbol{\mathcal{V}}\right)_P + \left(\frac{\mu}{\eta}\boldsymbol{\sigma}, \boldsymbol{\mathcal{V}}\right)_P + c\left(\mathcal{L}_{\boldsymbol{f}}\boldsymbol{\sigma}, \boldsymbol{\mathcal{V}}\right) \right] \mathrm{d}t \int_0^T F_2(\boldsymbol{\mathcal{V}})\ \mathrm{d}t, \tag{A.49}$$

using the initial condition for approximation (A.21b).

By comparison the equations (A.47) and (A.49), and because we could choose $\boldsymbol{\mathcal{V}}(0)$ arbitrarily, we get a fulfillment of the initial condition $\boldsymbol{\sigma}(0) = 0$.

Step 5: Uniqueness of $\boldsymbol{\sigma}$, $\boldsymbol{u}$ and $\boldsymbol{\tau}$

We will use a similar idea as in the proof of the uniqueness of the solution of the elastic problem. We choose two different slip functions $\boldsymbol{f}_1 \neq \boldsymbol{f}_2$ and show that if they have equal trace on boundary Γ then the solutions hold $\boldsymbol{\sigma}_1 = \boldsymbol{\sigma}_2$, $\boldsymbol{u}_1 = \boldsymbol{u}_2$ and $\boldsymbol{\tau}_1 = \boldsymbol{\tau}_2$.

First, we subtract these functions and denote their difference as $\boldsymbol{f}$. We thus obtain $T_\Gamma \boldsymbol{f} = 0$ and $\boldsymbol{f} \in V$. Employing the Galerkin method we get the existence of $\boldsymbol{\sigma}_1$, $\boldsymbol{\sigma}_2$, $\overline{\boldsymbol{u}}_1$ and $\overline{\boldsymbol{u}}_2$, for which we rewrite the equations (4.6) and subtract them as follows

$$a\left(\overline{\boldsymbol{u}}_1 - \overline{\boldsymbol{u}}_2, \boldsymbol{U}\right) + b\left(\overline{\boldsymbol{u}}_1 - \overline{\boldsymbol{u}}_2, \boldsymbol{U}\right) + \left(\boldsymbol{\sigma}_1 - \boldsymbol{\sigma}_2, \boldsymbol{\varepsilon}(\boldsymbol{U})\right)_P = F_1(\boldsymbol{U}) \quad \forall \boldsymbol{U} \in V \tag{A.50a}$$

$$\left(\partial_t(\boldsymbol{\sigma}_1 - \boldsymbol{\sigma}_2), \boldsymbol{\mathcal{S}}\right) + \left(\frac{\mu}{\eta}\boldsymbol{\sigma}_1 - \boldsymbol{\sigma}_2, \boldsymbol{\mathcal{S}}\right)_P + c\left(\overline{\boldsymbol{u}}_1 - \overline{\boldsymbol{u}}_2, \boldsymbol{\mathcal{S}}\right) = F_2(\boldsymbol{\mathcal{S}}) \quad \forall \boldsymbol{\mathcal{S}} \in P \tag{A.50b}$$

for a.e. $\mathrm{t} \in (0, T)$.

The function $\boldsymbol{f} \in V$ occurs in the forms $F_1(\cdot)$ and $F_2(\cdot)$ and because they are also linear, we can rewrite them to the bilinear forms $a(\cdot,\cdot)$, $b(\cdot,\cdot)$ and $c(\cdot,\cdot)$

$$a\left(\boldsymbol{u}_1-\boldsymbol{u}_2,\boldsymbol{U}\right)+b\left(\boldsymbol{u}_1-\boldsymbol{u}_2,\boldsymbol{U}\right)+\left(\boldsymbol{\sigma}_1-\boldsymbol{\sigma}_2,\boldsymbol{\varepsilon}(\boldsymbol{U})\right)_P=0 \qquad \forall \boldsymbol{U}\in V \tag{A.51a}$$

$$\left(\partial_t(\boldsymbol{\sigma}_1-\boldsymbol{\sigma}_2),\boldsymbol{\mathcal{S}}\right)+\left(\frac{\mu}{\eta}\boldsymbol{\sigma}_1-\boldsymbol{\sigma}_2,\boldsymbol{\mathcal{S}}\right)_P+c\left(\boldsymbol{u}_1-\boldsymbol{u}_2,\boldsymbol{\mathcal{S}}\right)=0 \qquad \forall \boldsymbol{\mathcal{S}}\in P \tag{A.51b}$$

for a.e. $\mathrm{t}\in(0,T)$.

When we use estimate (A.14), we get boundedness from the equation (A.51a)

$$\left\|\boldsymbol{u}_1-\boldsymbol{u}_2\right\|_V\leq C\left\|\boldsymbol{\sigma}_1-\boldsymbol{\sigma}_2\right\|_P \qquad \text{for a.e. } \mathrm{t}\in(0,T). \tag{A.52}$$

When we put the test function $\boldsymbol{\mathcal{S}}:=\boldsymbol{\sigma}_1-\boldsymbol{\sigma}_2$ to the equation (A.51b) we get

$$\frac{\mathrm{d}}{\mathrm{d}t}\left(\frac{1}{2}\left\|\boldsymbol{\sigma}_1-\boldsymbol{\sigma}_2\right\|_P^2\right)+\left(\frac{\mu}{\eta}(\boldsymbol{\sigma}_1-\boldsymbol{\sigma}_2),(\boldsymbol{\sigma}_1-\boldsymbol{\sigma}_2)\right)_P+c\left(\boldsymbol{u}_1-\boldsymbol{u}_2,\boldsymbol{\sigma}_1-\boldsymbol{\sigma}_2\right)=0. \tag{A.53}$$

From the inequalities (A.26),(A.28) and (A.52) we obtain an estimate

$$\frac{\mathrm{d}}{\mathrm{d}t}\left(\left\|\boldsymbol{\sigma}_1-\boldsymbol{\sigma}_2\right\|_P^2\right)\leq C\left\|\boldsymbol{\sigma}_1-\boldsymbol{\sigma}_2\right\|_P^2 \qquad \text{for a.e. } \mathrm{t}\in(0,T). \tag{A.54}$$

Now we use the Gronwall lemma in the differential form and because of zero initial conditions for $\boldsymbol{\sigma}_1$ and $\boldsymbol{\sigma}_2$ we get

$$\left\|\boldsymbol{\sigma}_1-\boldsymbol{\sigma}_2\right\|_P^2\leq 0 \quad \text{ which imply } \quad \boldsymbol{\sigma}_1=\boldsymbol{\sigma}_2, \tag{A.55}$$

We also obtain $\boldsymbol{u}_1=\boldsymbol{u}_2$ from the equation (A.51a) as well as the uniqueness of $\boldsymbol{\tau}$ from Hooke's law.

Step 6: Spaces of the other unknowns

Eventually, the question arises, in what spaces the other unknowns lie. From the inequality (A.14) for $\overline{\boldsymbol{u}}$ we get directly $\overline{\boldsymbol{u}}\in L^2\left((0,T);V\right)$, however we can even show that this unknown is continuous in time. We put down equation (4.6a) for two displacements in different times t_1 and t_2, and taking into account that the slip function is constant in time, we get

$$a\left(\overline{\boldsymbol{u}}(t_1)-\overline{\boldsymbol{u}}(t_2),\boldsymbol{U}\right)+b\left(\overline{\boldsymbol{u}}(t_1)-\overline{\boldsymbol{u}}(t_2),\boldsymbol{U}\right)+\left(\boldsymbol{\sigma}(t_1)-\boldsymbol{\sigma}(t_2),\boldsymbol{\varepsilon}(\boldsymbol{U})\right)_P=0, \tag{A.56}$$

which holds for $\forall \boldsymbol{U} \in V$. If we use again the estimate (A.14), we obtain the following displacement restriction

$$\|\overline{\boldsymbol{u}}(t_1) - \overline{\boldsymbol{u}}(t_2)\|_V \leq C \, \|\boldsymbol{\sigma}(t_1) - \boldsymbol{\sigma}(t_2)\|_P \,, \tag{A.57}$$

where the constant C is time independent. If we consider now that $\boldsymbol{\sigma} \in \mathcal{C}\left([0,T];P\right)$ and also that we have explicit equation for the strain $\boldsymbol{\tau}$, we can immediately write

$$\overline{\boldsymbol{u}} \in \mathcal{C}\left([0,T];V\right), \quad \boldsymbol{\tau} \in \mathcal{C}\left([0,T];P\right). \tag{A.58}$$

We can also get the norm estimates similarly as in the case (A.46).

References

Boschi, L., Piersanti, A., Spada, G., 2000. Global postseismic deformation: Deep earthquakes, *J. Geophys. Res.*, 105: 631–652.

Bramley, R., Wang, X., 1997. SPLIB: A library of iterative methods for sparse linear systems *Department of Computer Science, Indiana University, Bloomington, IN* `http://www.cs.indiana.edu/ ftp /bramley/ splib.tar.gz`

Cesca, S., Vermeersen, L.L.A., Sabadini, R., 2000. Influence of lithospheric and mantle stratification on co- and post-seismic deformation due to finite faults, *Geophys. J. Intern.*, 143: 575–581.

Cianetti, S., Giunchi, C., Cocco, M., 2005. Three-dimensional finite element modeling of stress interaction: An application to Landers and Hector Mine fault systems, *J. Geophys. Res.*, 110: B05S17.

Dahlen, F.A., Tromp, J., 1998. Theoretical Global Seismology, *Princeton Univ. Press, Princeton.*

Dziewonski, A.M., Anderson, D.L., 1981. Preliminary reference Earth model, *Phys. Earth Planet. Inter.*, 25: 297–356.

Evans, L.C.,1998. Partial Differential Equations, *Amer. Math. Society*, Providence.

Hetland, E.A., Hager, B.H., 2005. Postseismic and interseismic displacements near a strike-slip fault: A two-dimensional theory for general linear viscoelastic rheologies, *J. Geophys. Res.*, 110: B10401.

Hron, J., Turek, S., 2006. A monolithic FEM/multigrid solver for an ALE formulation of fluid-structure interaction with applications in biomechanics. *In: Bungartz, Schfer, (Eds.), Fluid-Structure Interaction, Lecture Notes in Computational Science and Engineering*, 53: pp. 146-170.

Hu, Y., Wang, K., He, J., Klotz, J., Khazaradze, G., 2004. Three-dimensional viscoelastic finite element model for postseismic deformation of the great 1960 Chile earthquake, *J. Geophys. Res.*, 109: B12403.

Inovecký, L., 2003. Postglacial Relaxation of the Earth's Models in Cylindrically Symmetric Geometry, Master Thesis, *MFF UK Prague.*

Karakostas, V.G., Papadimitriou, E.E., Papazachos, C.B., 2004. Properties of the 2003 Lefkada, Ionian Islands, Greece, Earthquake Seismic Sequence and Seismicity Triggering, *Bull. Seism. Soc. Am.*, 94: 1976–1981.

King, G.C.P., Cocco, M., 2001. Fault interaction by elastic stress changes: New clues from earthquake sequences *ADV GEOPHYS.*

Melini, D., Piersanti, A., Spada, G., Soldati, G., Casarotti, E., Boschi, E., 2004. Earthquake and relative sealevel changes, *Geophys. Res. Lett.*, 31: L09601.

Nečas, J., Hlaváček, I., 1981. Mathematical Theory of Elastic and Elastoplastic Bodies: An Introduction, *Elsevier, Amsterdam.*

Nostro, C., Piersanti, A. Cocco, M., 2001. Normal fault interaction caused by coseismic and postseismic stress changes, *J. Geophysic. Res.*, 106: 19391–19410.

Pergler, T., 2004. Postseismická relaxace modelů Země s Maxwellovskou reologií, Master Thesis in Czech language, *MFF UK Prague.*

Piersanti, A., Spada, G., Sabadini, R., Bonafede, M., 1995. Global postseismic deformation, *Geoph. J. Intern.*, 120: 544–566.

Piersanti, A., Spada, G., Sabadini, R., 1997. Global postseismic rebound of a viscoelastic Earth: Theory for finite faults and application to the 1964 Alaska earthquake, *J. Geophys. Res.*, 102: 477-492.

Pollitz, F.F., 1992. Postseismic relaxation theory on the spherical earth, *Bull. Seism. Soc. Am.*, 82: 422–453.

Pollitz, F.F.,1997. Gravitational viscoelastic postseismic relaxation on a layered spherical Earth, *J. Geophys. Res.*, 102: 17921–17941.

Pollitz, F.F., 2003. Post-seismic relaxation on a laterally heterogeneous viscoelastic model, *Geophys. J. Intern.*, 155: 57–78.

Sabadini, R., Vermeersen, L.L.A., 1997. Influence of lithospheric and mantle stratification on global post-seismic deformation, *Geophys. Res. Lett.*, 24: 2075–2078.

Singh, S.J., Rani, S., 1993. Crustal deformation associated with 2-dimensional thrust faulting, *J. Physics of the Earth*, 41: 87–101.

Singh, S.J., Rani, S., 1994. Modeling of coseismic and postseismic crustal deformation associated with strike-slip faulting, *Current Science*, 66: 219–223.

Singh, S.J., Singh, M., 2004. Deformation of a layered half-space due to a very long tensile fault, *Proceed. Indian Acad. Sc.-Earth and Plan. Sc.*, 113: 235-246.

Soldati, G., Piersanti, A., Boschi, E., 1998. Global postseismic gravity changes of a viscoelastic earth, *J. Geophys. Res.*, 103: 29867-29885.

Soldati, G., Boschi, L., Piersanti, A., Spada, G., 2001. The effect of global seismicity on the polar motion of a viscoelastic Earth, *J. Geophys. Res.*, 106: 6761–6767.

Suito, H., Hirahara, K., 1999. Simulation of postseismic deformations caused by the 1896 Riku-u Earthquake, Northeast Japan: Re-evaluation of the viscosity in the upper mantle, *Geophys. Res. Lett.*, 26: 2561–2564.

Suito, H., Iizuka, M., Hirahara, K., 2002. 3-D viscoelastic FEM Modeling of crustal deformation in northeast Japan, *Pure and Appl. Geophys.*, 159: 2239–2259.

Sun, W.K., Okubo, S., 2002. Effect of earth's spherical curvature and radial heterogeneity in dislocation studies - for a point dislocation, *Geophysic. Res. Lett.*, 29: 1605.

Sun, W.K., 2004. Asymptotic solution of static displacements caused by dislocations in a spherically symentric Earth, *J. Geophys. Res.*, 109: B05402.

Teisseyre, R., 1986. Continuum Theories in Solid Earth Physics, *PWN & Elsevier, Warszawa.*

Xing, H.L., Mora, P., 2006. Construction of an Intraplate Fault System Model of South Australia, and Simulation Tool for the iSERVO Institute Seed Project, *Pure and Appl. Geophys.*, 163: 2297–2316.

Xing, H.L., Mora, P., Makinouchi, A., 2006. A unified friction description and its application to the simulation of frictional instability using the finite element method *Philosophical Magazine*, 86: 3453-3475.

Yoshioka, S., Tokunaga, Y.O., 1998. Numerical simulation of displacement and stress fields associated with 1993 Kushiro-oki, Japan, earthquake, *Pure and Appl. Geophys.*, 152: 443–464.

Yoshioka, S., Suzuki, H., 1999. Effect of three-dimensional inhomogeneous viscoelastic structures on postseismic surface deformation associated with the great 1946 Nankaido earthquake, *Pure and Appl. Geophys.*, 154: 307–328.

Yu, T.T., Rundle, J.B., Fernandez, J., 1996. Surface deformation due to a strike-slip fault in an elastic gravitational layer overlying a viscoelastic gravitational half-space, *J. Geophys. Res.*, 101: 3199–3214.

Zahradník J., Serpetsidaki A., Sokos E., Tselentis G.A., 2005. Iterative deconvolution of regional waveforms and a double-event interpretation of the 2003 Lefkada earthquake, Greece. *Bull. Seism. Soc. Am.*, 95: 159–172.

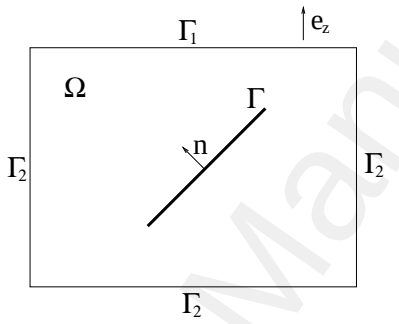

Figure 1: Vertical cross-section of a 3D domain Ω. Boundary Γ_1 denotes the surface of the Earth, Γ_2 are the boundaries of the area under the Earth's surface and the fault is denoted by Γ.

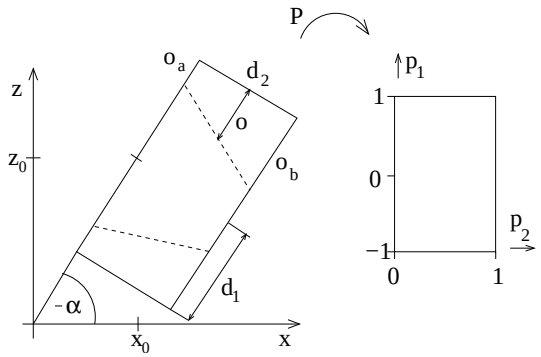

Figure 2: Mapping $P : (x, z) \rightarrow (p_1, p_2)$

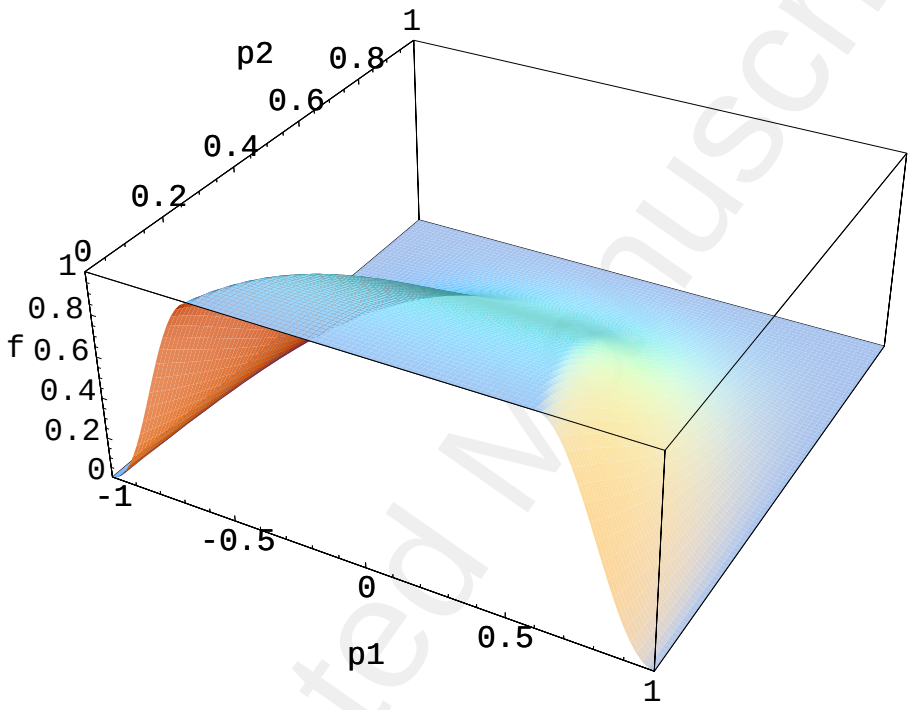

Figure 3: Scalar function f on unit domain with coordinates p_1 and p_2.

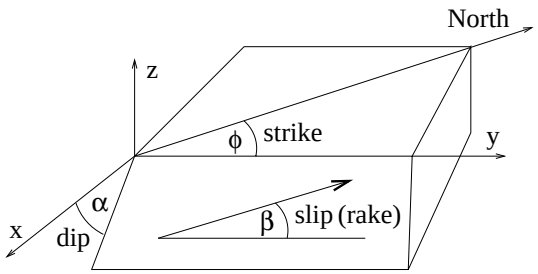

Figure 4: Fault location is determined by these three angles.

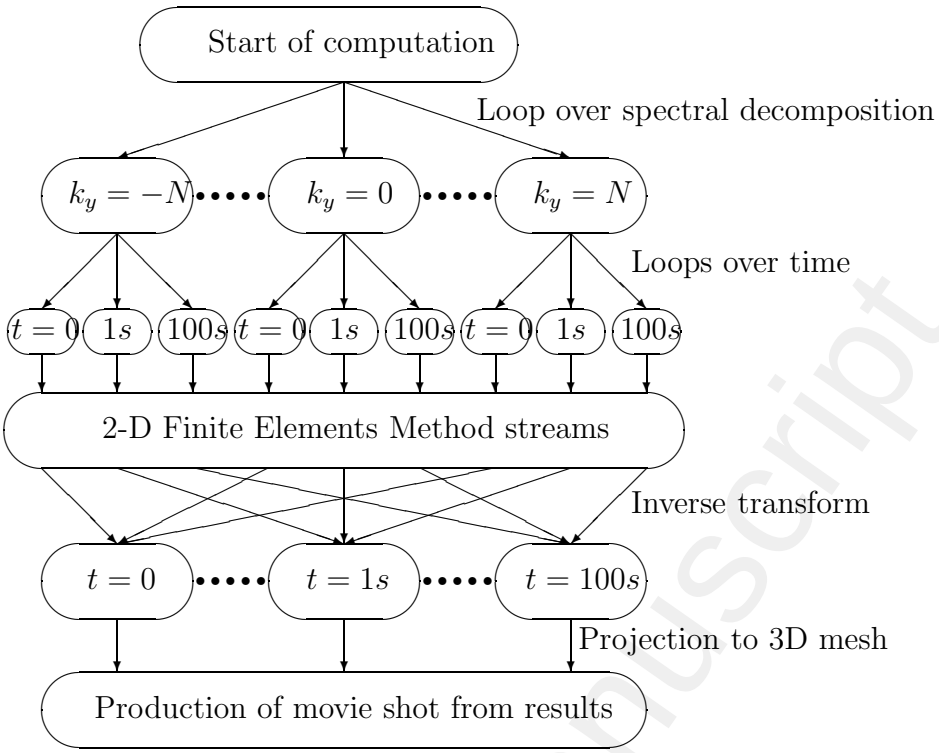

Figure 5: Float chart of the numerical method.

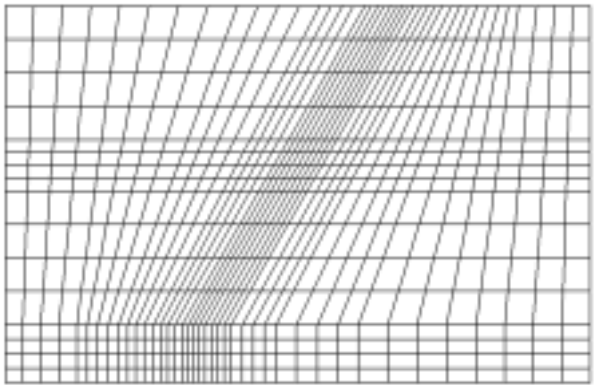

(a) Adapted mesh

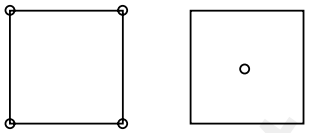

(b) Elements for the displacements $\boldsymbol{u}_i$ and the stresses $\boldsymbol{\tau}_i$

Figure 6: Finite elements

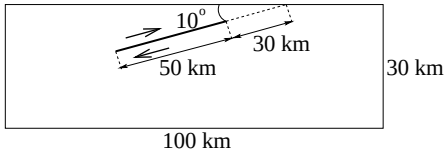

(a) The geometry of dip-slip fault.

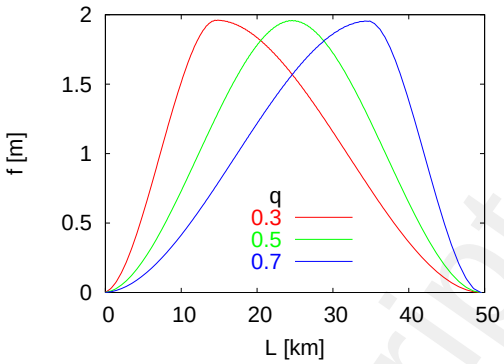

(b) Scalar rupture function f for three different value of parameter q. x-axis is oriented along the rupture and the distance L is measured from the upper end of the fault.

Figure 7: Definition of the 2-D example from Teisseyre (1986).

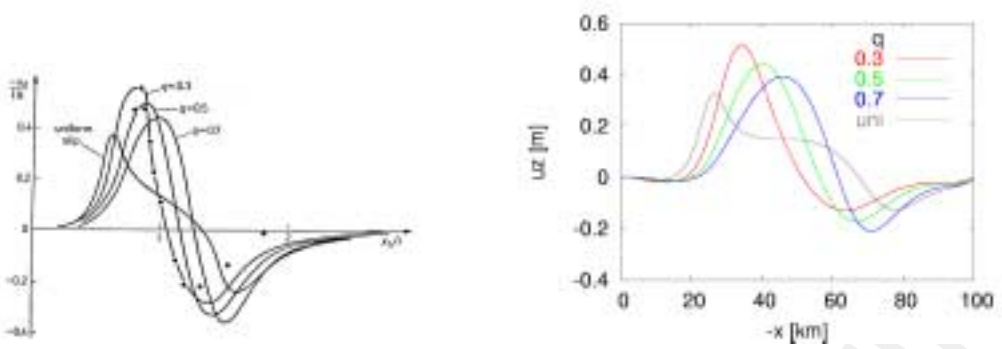

(a) Results from Teisseyre (1986) (b) Results computed by our method

Figure 8: Surface vertical displacements u_z for three different values of parameter q and uniform slip. On the x-axis is distance from imaginary intersection of fault tangential vector and Earth surface.

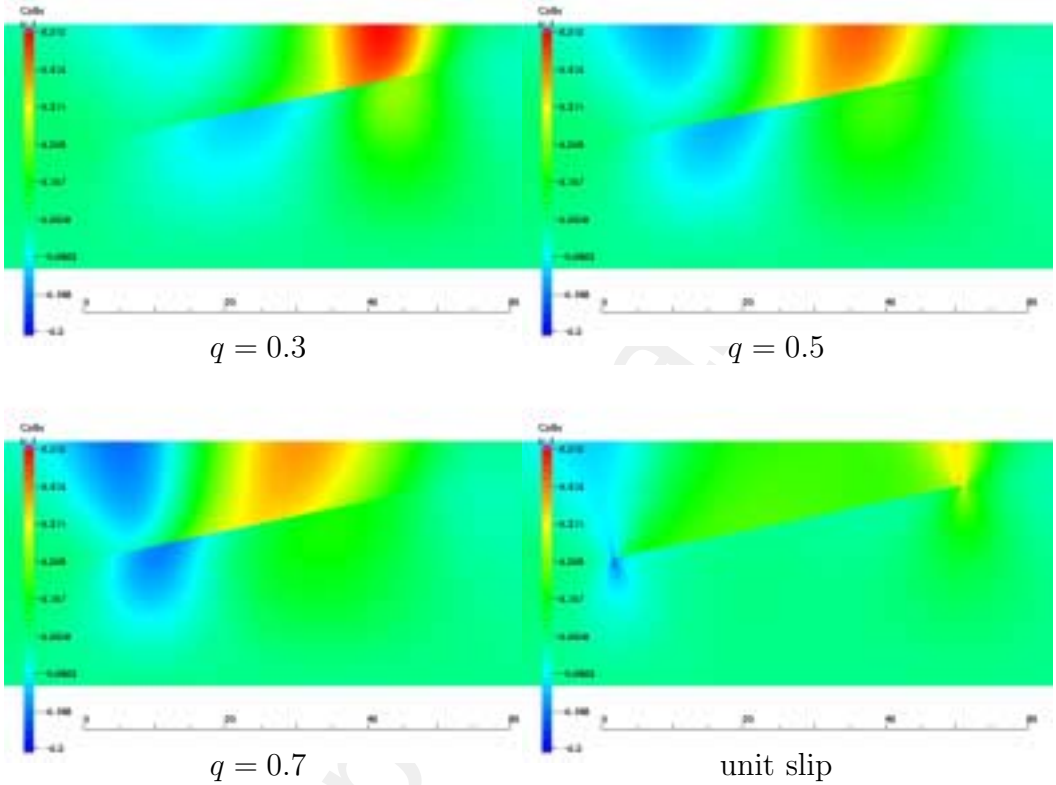

$q = 0.3$ $q = 0.5$

$q = 0.7$ unit slip

Figure 9: Vertical displacement u_z[m] on domain Ω for three different values of parameter q and for uniform slip. The scale is in km.

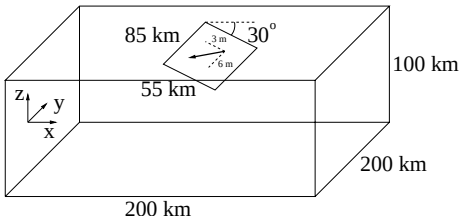

Figure 10: Model geometry. The slip on the fault is schematically shown in the small rectangle

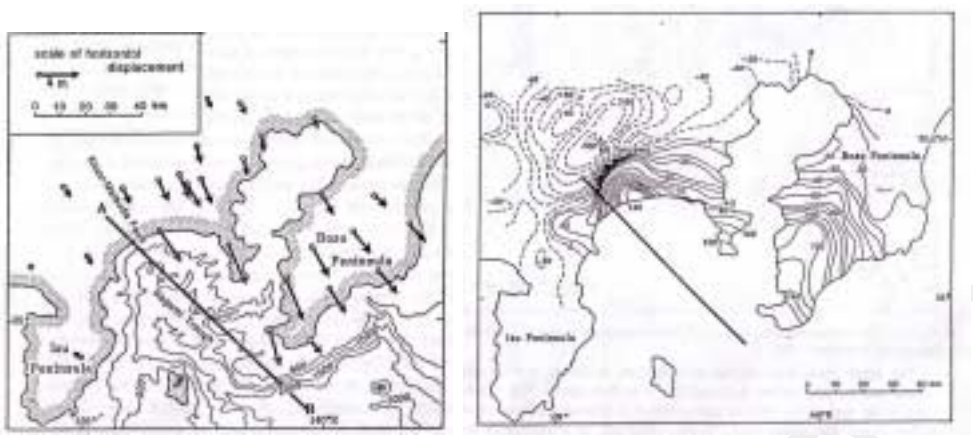

Observed values

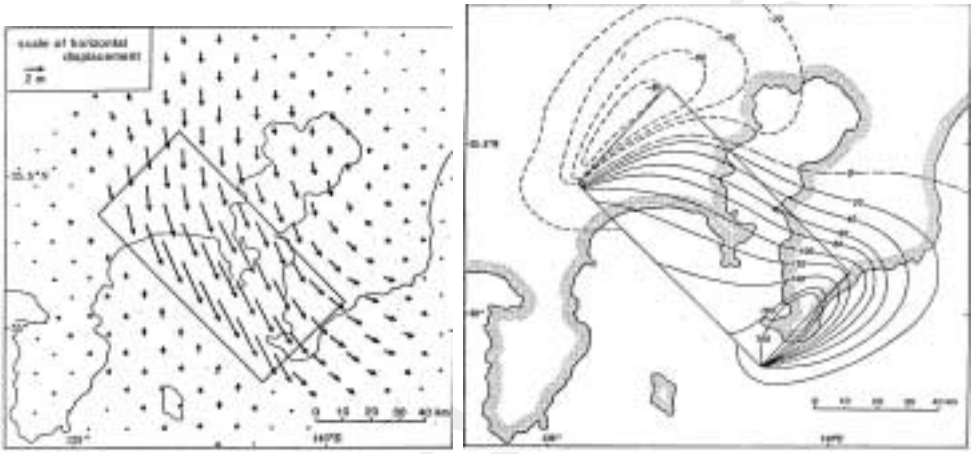

Calculated values according to the model presented in Teisseyre (1986)

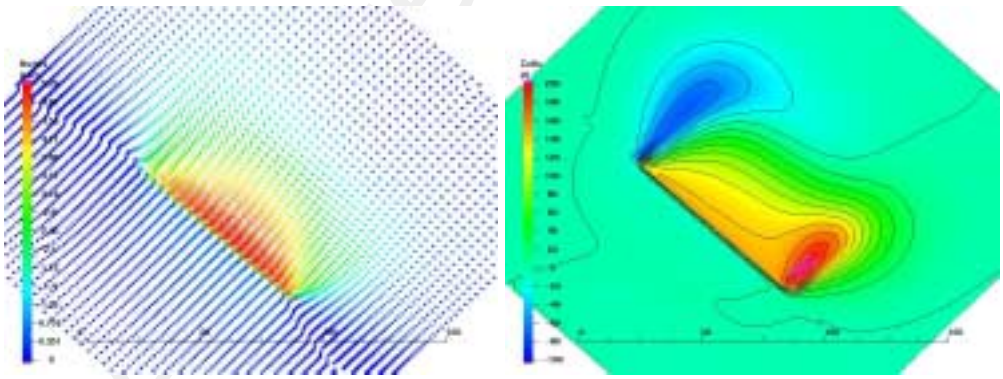

Results from our hybrid method (FEM+Fourier transform)

Figure 11: Horizontal and vertical displacements. On the left figures, the arrows show the sizes and directions of the horizontal displacements (scale is in m), on the right figures, the vertical displacements are presented with scale in cm.

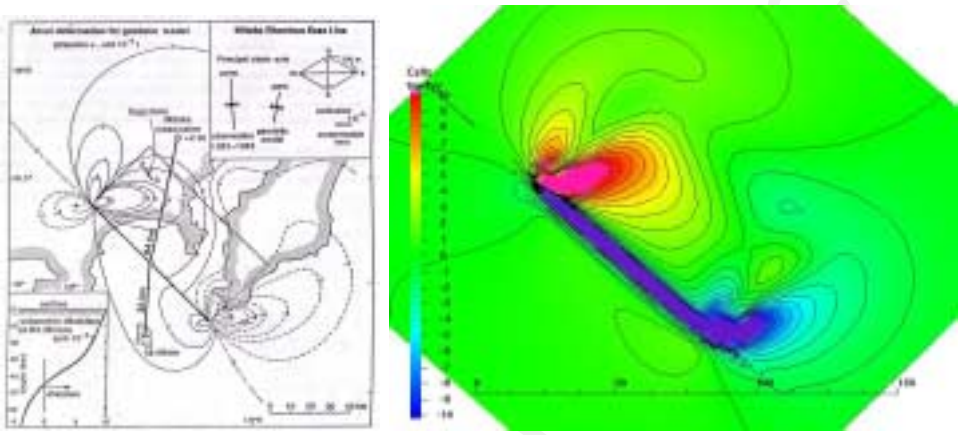

Figure 12: Surface strain changes $\tau_{xx} + \tau_{yy}$ in MPa. The left figure shows the result from Teisseyre (1986) and the right figure shows the result from our hybrid method.

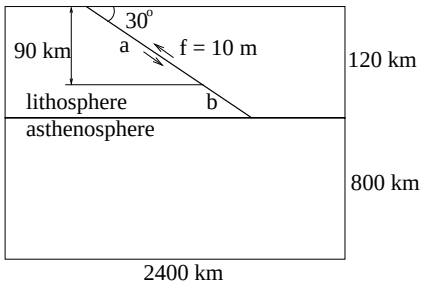

Figure 13: The model geometry, a and b denote two different sizes of the faults.

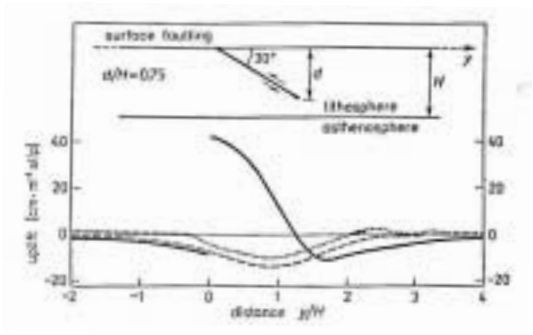

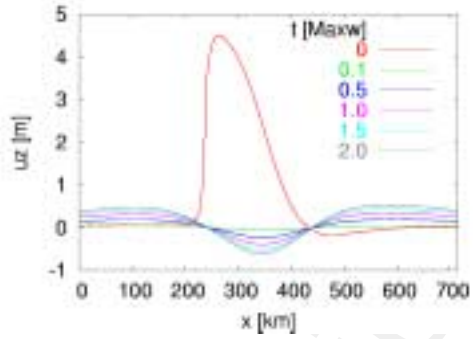

fault (a)

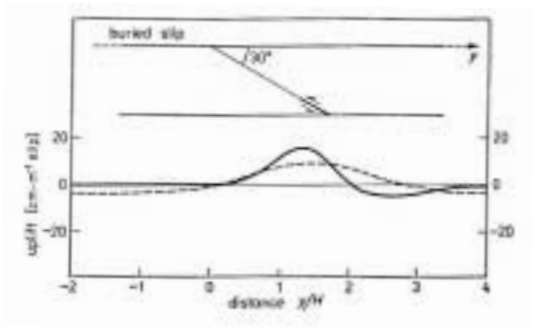

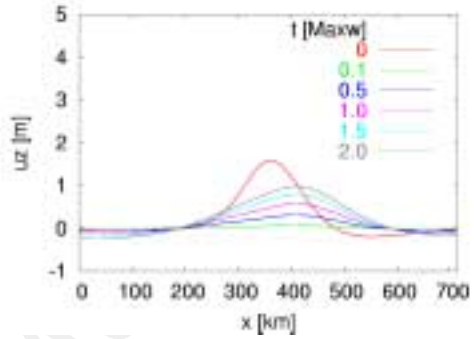

fault (b)

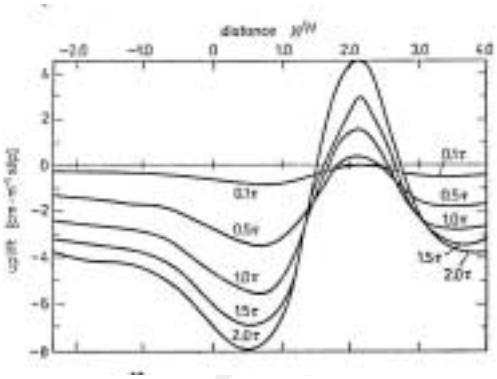

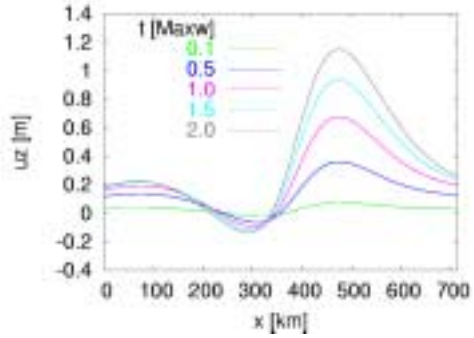

fault (c)

Figure 14: Coseismic and postseismic vertical surface displacement. On the left figures the plots from Teisseyre (1986) are presented, on the right figures our results are shown. The plots, taken for the cases (a) and (b), shows the elastic displacements in time $t = 0$ (denoted by solid lines) and viscoelastic displacements in time $t = 2\tau$ (dashes lines). From all the viscoelastic results for $t \neq 0$ the elastic displacements are subtracted. In the case (c), in which the fault is composed together from faults (a) and (b), only the viscoelastic displacements are presented. The considered values are $H = 120$ km and $|f| = 10$ m.

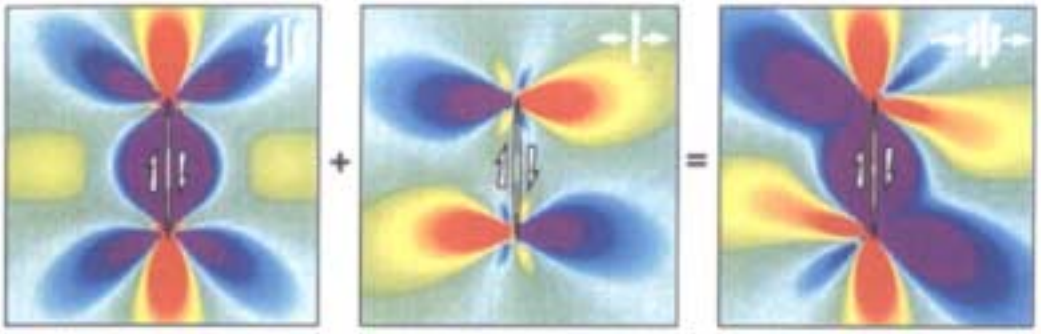

Figure 15: From the left, shear stress change $\Delta\tau = \boldsymbol{t} \cdot \boldsymbol{\tau} \cdot \boldsymbol{n}$, normal stress change $\Delta\sigma = \boldsymbol{n} \cdot \boldsymbol{\tau} \cdot \boldsymbol{n}$ and Coulomb stress ΔCFF, are presented. These figures are taken from King and Cocco (2001).

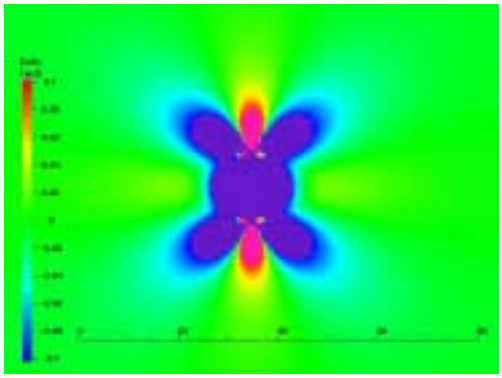

Shear stress change $\Delta\tau$

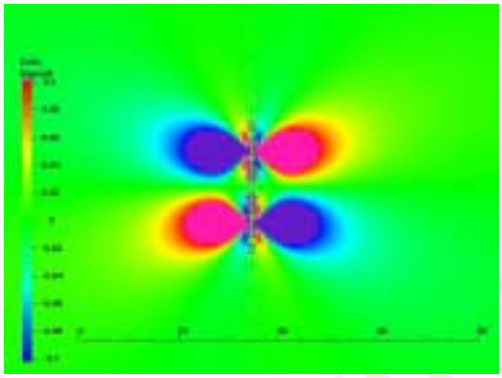

Normal stress change $\Delta\sigma$

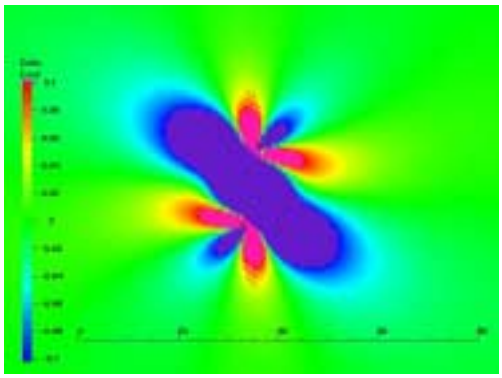

Coulomb stress ΔCFF

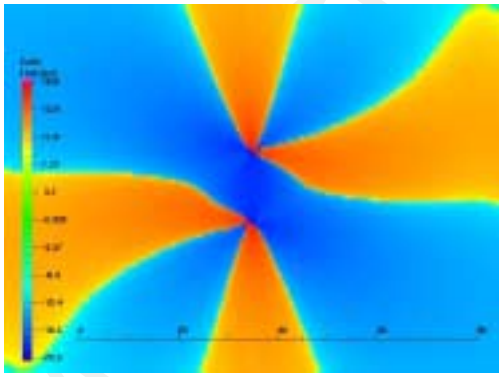

Coulomb stress ΔCFF in logarithmic scale (not in MPa).

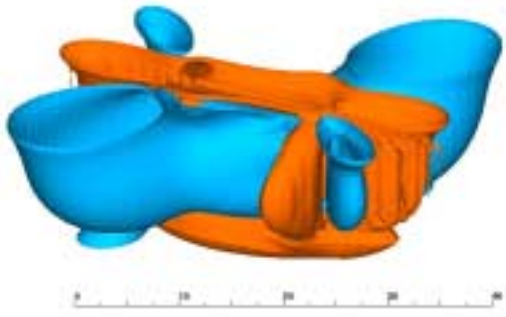

Isosurfaces of constant Coulomb stress, the blue isosurface denotes $\Delta CFF = -0.1$ MPa, the red isosurface denotes $\Delta CFF = 0.1$ MPa.

Figure 16: Results of Coulomb stresses (values are in MPa). The distance scales are given in km.

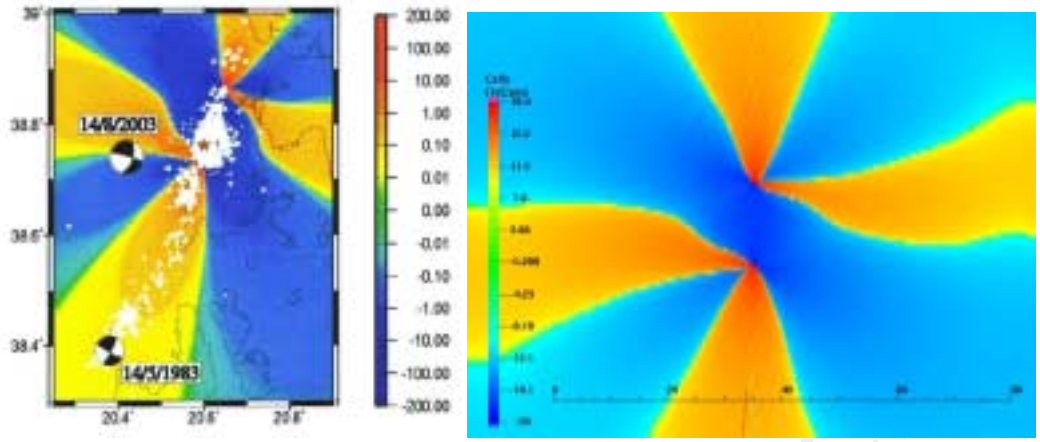

(a) Result from Karakostas et al. (2004), it is placed according to longitude and latitude of real fault (the scale is in 10^5 Pa).

(b) Our results without the right inclination of the fault. The distance scale is in km. On the bottom of the figure is marked the Cephalonia fault.

Figure 17: Incremental Coulomb stress ΔCFF in the depth of the middle of the Lefkada fault (7.5 km). The scale is logarithmic.

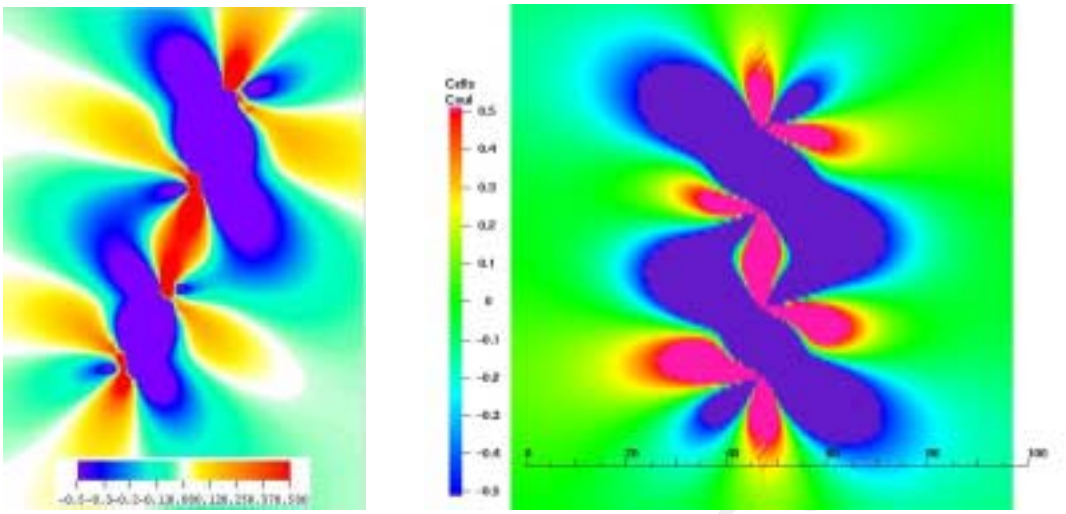

(a) The result presented by Suleyman Nalbant (personal contact), the faults are inclined according to the Earth coordinates.

(b) Our result without right inclination. The distance scale is in km.

Figure 18: Incremental Coulomb stress ΔCFF in the depth of the middle of the broken faults (7.5 km). The scales are in 10^5 Pa.

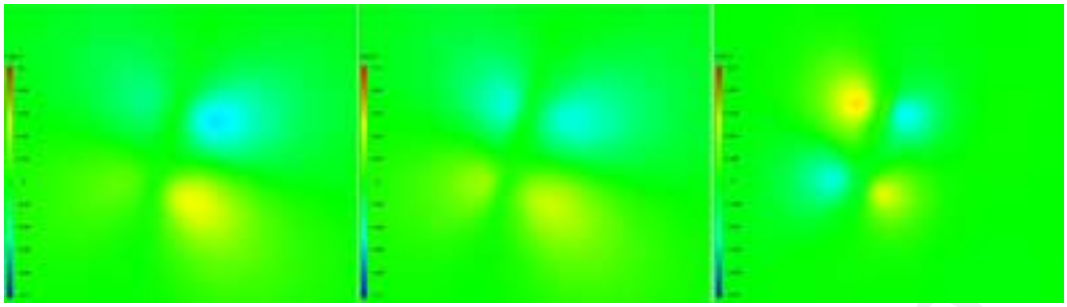

Horizontal displacement u_x

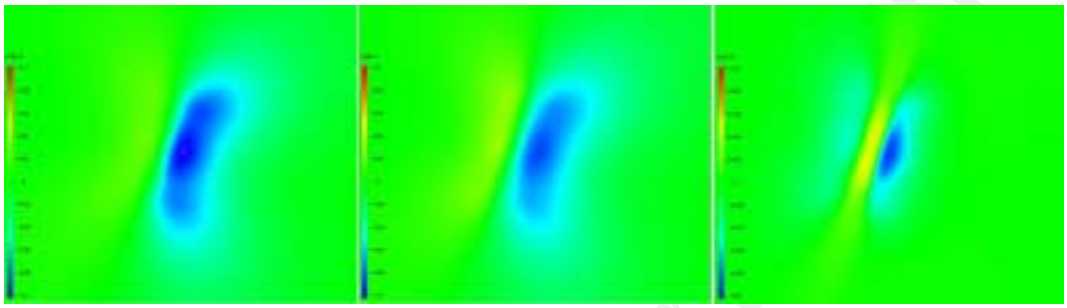

Horizontal displacement u_y

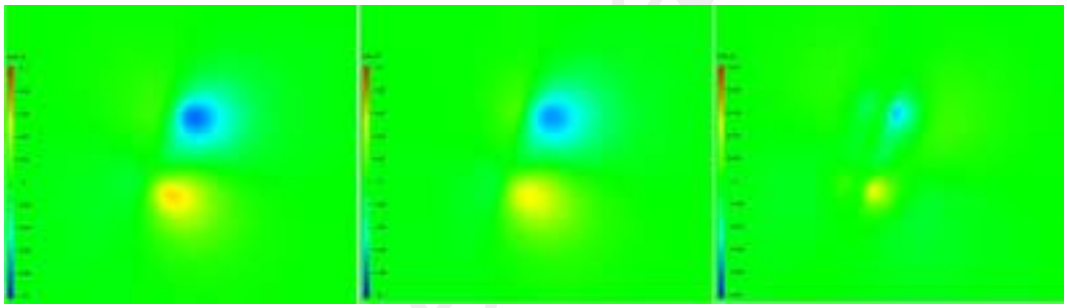

Vertical displacement u_z

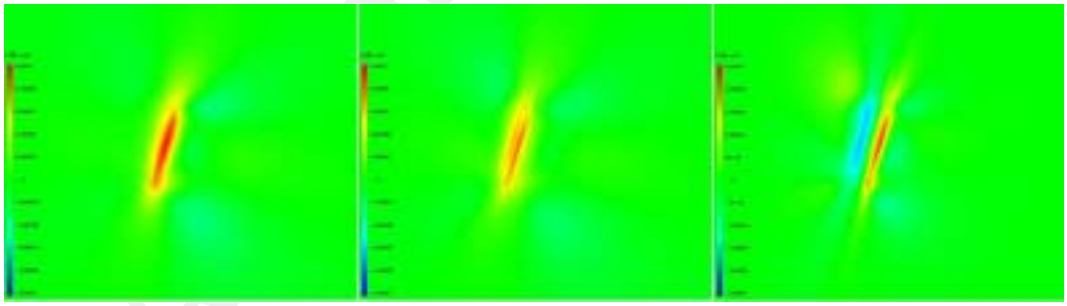

Coulomb stress

Figure 19: Surface displacements and surface Coulomb stress for the Lefkada earthquake. In the left column there are the results for a model with a flat surface, the middle column corresponds to the model with a non-flat topography and the right column shows the differences between the both models. The fault has a real Earth inclination. Displacement scales are in meters and the stress scales are in MPa. The scales in the right column are different.